THESIS FOR THE DEGREE OF LICENTIATE OF ENGINEERING

Coherent plasmon-plasmon and plasmon-exciton interactions at the nanoscale

MARTIN WERSÄLL

Department of Applied Physics

CHALMERS UNIVERSITY OF TECHNOLOGY

Gothenburg, Sweden 2015

Coherent plasmon-plasmon and plasmon-exciton interactions at the nanoscale

MARTIN WERSÄLL

Department of Applied Physics

Chalmers University of Technology

SE-412 96 Göteborg

Sweden

Telephone +46 (0)317721000

Cover:

(Top left) Directional asymmetric Au nanodimers, which supports directional scattering. (Top right) Molecular structure of TDBC and biotin. (Down left) Schematic drawing of surface electron cloud displacement at localized surface plasmon resonances. (Down right) Ag nanoprisms on top of a sheet of J-aggregated dye molecules.

Chalmers reproservice

Gothenburg, Sweden 2015

Coherent plasmon-plasmon and plasmon-exciton interactions at the nanoscale

Martin Wersäll
Department of Applied Physics
Chalmers University of Technology

Abstract

Noble metallic nanoparticles which supports localized surface plasmon resonances, offers a variety of potential scientific as well as industrial applications. Due to a remarkable ability to confine light at nanoscale dimensions, far below the optical diffraction limit, together with an ability to detect minute changes in the local environment plasmonic nanoparticles have paved routes towards several new and intriguing techniques, promising for future applications in areas such as molecular sensing and quantum optics.

The exploitation of coherent interations at the nanoscale is rather frequent in the scientific community, and has recently resulted in several prominent discoveries, which have ended up as publications in high-ranked scientific journals. However, numerous studies demonstrates utilization of coherent interactions in rather complicated systems, which is often costly and impractical for future development. Plenty of the phenomena presented within these studies are moreover based on measurements on an ensemble level, where there is either no or very limited knowledge in the performance of single nanoparticles. In this thesis we first present and demonstrate ways to acheive ultracompact and competitive molecular analysis in nanosized systems, which supports directional scattering properties due to coherent plasmon-plasmon interactions. Secondly we also demonstrates realization of strong light-matter interactions from plasmon-exciton coupling in nanosized systems comprised by single crystalline Ag nanoprisms and J-aggregated molecular sheets of TDBC. These demonstrations support promising outlooks for future plasmonic molecular analysis as well as room temperature quantum plasmonics and quantum optics.

Keywords: *localized surface plasmon resonances, strong coupling, directional emission, coherent interactions*.

APPENDED PAPERS

The following papers are included in this thesis:

Paper I:

Directional Nanoplasmonic Antennas for Self-referenced Refractometric Molecular Analysis

M. Wersäll, R. Verre, M. Svedendahl, P. Johansson, M. Käll and T. Shegai

The Journal of Physical Chemistry C **2014**, 118, 21075-21080

Paper II:

Realizing Strong Light-Matter Interactions between Single-Nanoparticle Plasmons and Molecular Excitons at Ambient Conditions

G. Zengin, **M. Wersäll**, S. Nilsson, T. J. Antosiewicz, M. Käll and T. Shegai

Physical Review Letters **2015**, 114, 157401

My contributions:

In **Paper I**, I helped design and construct the optical system with the ability to measure ratio of left/right-scattered intensities. All experimental measurements and the initial manuscript were conducted and was written by myself.

In **Paper II**, I helped devising and measuring all single particle-dye dark-field scattering spectra. Moreover I helped correlating all scattering spectra with SEM images. I helped analyse all data and also co-wrote the manuscript.

Contents

Chapter 1

Introduction

The interaction between light and matter has been a source of mystery and excitement throughout history. Attempts in developing a theory to describe the underlying dynamics of light-matter interactions were made already in ancient Greece by the pre-Soctratic philosopher Empedocles (490-430 BC) [1]. Even though theories have advanced and progressed during the elapse of time, the fundamental nature of light and hence light-matter interactions is still a subject for debate among scientists.

Ever since the birth of quantum mechanics, scientists have been able to deduce theoretical outcomes which match optical experimental observations in a satisfying manner. This has resulted in many essential inventions in the 20th century such as laser, light-emitting diods (LEDs) and photovoltaics [2-4]. Even though the theoretical foundations work well enough to predict experimental outcomes in a satisfoctory manner, the philisophical interpretation of quantum dynamics remains a debated matter among scientists [5-6].

Since visible light has a wavelength in the range of 390-700 nanometers it was previously widely regarded that it was a mere impossibility to focus light to spatial dimensions much smaller than the resolution limit, dictated by Abbe's criterion (Ernst Abbe is a 19th century physicist) [7]. All this changed with the introduction of surface plasmon resonances (SPR), were visible light couple strongly to collective oscillation of charge densities in nanoscale entities of noble metals [8]. The discovery of surface plasmons eventuated in completely new possibilities to affect and manipulte light at spatial nanoscale dimensions. In addition, the surface charge density oscillations associated with surface plasmons, at the interafce between the metal and the dielectric environment, lead to strongly enhanced optical evanescent fields [9]. This make them highly susceptible to changes in the local dielectric environment. The introduction of surface plasmons furthermore resulted in a completely new scientific era in optics and nanotechnology. It led to several new ideas on how to exploit light-matter interactions to acheive efficient energy harvesting, molecular sensing and new and intriguing nano optics [10], to name a few. Since the discovery of surface plasmons it has also been a progress in nanofabrication and sample manufacturing. For instance, techniques such as hole-mask colloidal lithography [11] and/or dropcasting colloidal nanoparticles suspended in solution on to a substrate, give the ability to create surfaces of several inches comprised by many separated distinct nanoscale structures. Moreover this is done in a very cost efficient manner, which makes such sample preparation techniques promising for the market.

In this thesis I will present possible ways of utilizing coherent light-matter interactions at the nanoscale to acheive the following goals:

1. *Constructing nanoscale plasmonic structures which supports directional scattering properties in order to perform single-wavelength self-referenced refractometric molecular analysis. We also aim to perform this by exploiting ultra-compact and cost efficient optical components.*

2. *Realizing strong coupling by utilizing single-particle plasmon-exciton interactions between a resonant plasmonic cavity and several quantum emitters at ambient conditions.*

Since many of the present plasmonic sensing schemes rely on expensive and complicated experimental equipment, such as spectrometers and stable light sources [12], a fulfillment of goal number 1 would imply that molecular plasmonic sensing could be performed in a simple, robust, cost efficient and ultra-compact manner. This opens up for future competitive plasmonic sensing devices, suitable for medical diagnostics at home without any authorized supervision.

Regarding goal number 2, recent studies have demonstrated strong coupling on an ensemble level or in various nanoparticle arrays or assemblies coupled to a large number of excitons [13-15]. Even though there have been a few demonstrations of strong light-matter interactions at the single-particle level [16-17], there still remain ambiguities in the interpretation of plasmon-exciton interactions presentet in these studies [18]. From a quantum optical perspective this indicates an uncertainty in the number of excitons involved in the interactions, as well as a question if plasmonic structures are capable of realizing strong light-matter interactions at its fundamental limit. Since questions of this kind are essential for quantum optics applications, it is of great importance to further investigate these issues [19-20]. By acheiving goal number 2 we will hence open up promising expectations for room temperature quantum plasmonics and quantum optics. Strongly coupled nanoscale systems are regarded as possible candidates in future quantum information processing networks, quantum cryptography and ultrafast single-photon switches [21-23] to name a few. This indicates that such components have the possibility to push society into a whole new scientific era.

In the beginning of this thesis several theorethical frameworks, that will be crucial for the performance of our goals, are presented and explained. Thereafter experimental data, supporting our outlined goals, are presented and analysed. Finally a quick summary and future outlooks are displayed and touched upon to describe possible routes of development.

Chapter 2

Coherent Interactions Between Dipole Emitters

The term coherence stems from the latin word *cohaerentia*, which means approximately *to unite* [24]. In the case of electromagnetic fields it refers to the correlation between two different fields and is mathematically quantified by the so-called *cross-correlation function* [25]. More generally optimal coherence imply constant intrinsic and spatial phase difference, as well as that waves emitted from the different sources acquire same frequency. The notion of coherence can be generalized to encapsulate a wide range of concepts such as energy states in the field of quantum optics and overall quantum mechanics.

2.1 Radiation from many coherently emitting dipoles

The resulting net radiation pattern from more than one oscillating dipole emitter may be derived by imposing the superposition principle. The radiated intensity from N coherently oscillating dipoles is expressed according to [7]

$$I \sim \left|\sum_{i=1}^{N} \boldsymbol{p}_i\right|^2 = \sum_{i=1}^{N} |\boldsymbol{p}_i|^2 + \sum_{i=1}^{N-1} \sum_{j=i+1}^{N} 2|\boldsymbol{p}_i||\boldsymbol{p}_j| \cos(\boldsymbol{k} \cdot \boldsymbol{R}_{ij} + \Delta\varphi_{ij}) \tag{2.1}$$

where $\boldsymbol{p}_i$ referres to the complex dipole moment vector of the i^{th} emitter and $\boldsymbol{R}_{ij} = \boldsymbol{R}_i - \boldsymbol{R}_j$ is a vector which magnitude and direction correspeonds to the distance and direction between i^{th} and j^{th} dipole sources. The corresponding intrinsic phase difference is further written as

$$\Delta\varphi_{ij} = \arctan\left(\frac{Re\{p_i\}Im\{p_j\} - Re\{p_j\}Im\{p_i\}}{Re\{p_i\}Re\{p_j\} + Im\{p_i\}Im\{p_j\}}\right) \tag{2.2}$$

The first term in expression (2.1) describes light emitted by individual dipoles and the second term depict interference between radiated fields originating from separate dipoles. If instead these sources were radiating in an incoherent manner the net intensity would exclusively be accounted for by the first term. Since the intrinsic phase difference between the sources then are completely random, all intrinsic phase differences would then be averaged out and no interference effects would take place. The illustrated situation is depicted in Figure 2.1 where the total radiation from each individual dipole give rise to a net radiating intensity, expressed by (2.1) together with (2.2).

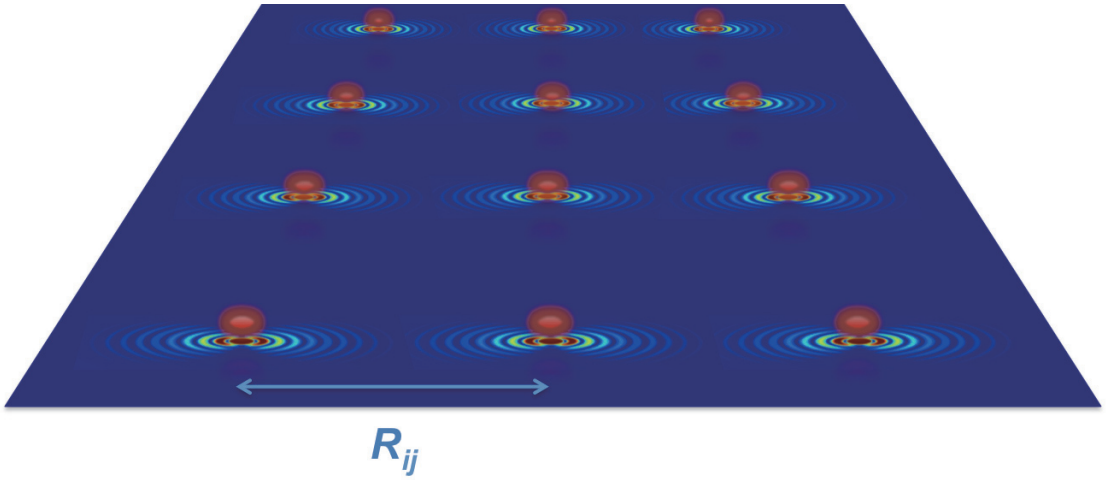

Figure 2.1: *Illustration of many dipolar emitters located on a two dimensional area. The radiation pattern from each individual dipole is projected on to the plane, which collectively forms a total radiation pattern dependent on intrinsic phase difference and intermediate spacing.*

2.2 Directional emission from a pair of detuned dipole emitters

To understand how directional emission occurs, conditions for interference of light originating from two different coherent point dipole sources may be investigated, as previously mentioned in Section 2.1. From phasor addition in the complex plane and/or calculating the time average (over a time period T) of the square of the electric field, the total intensity at a radial distance R away from the radiating dipole may be expressed as [7]

$$I = \langle |\boldsymbol{E}|^2 \rangle_T \approx \frac{1}{16\pi^2 \varepsilon_0^2 R^2} (|\boldsymbol{p}_1|^2 + |\boldsymbol{p}_2|^2 + 2|\boldsymbol{p}_1||\boldsymbol{p}_2| \cos(\boldsymbol{k} \cdot \boldsymbol{R}_{12} + \Delta\varphi_{12})) \quad (2.3)$$

Here $|\boldsymbol{p}_1|$, $|\boldsymbol{p}_2|$ and $\Delta\varphi_{12}$ are magnitudes and intrinsic phase difference of the dipoles respectively, $\boldsymbol{k} = \frac{2\pi n}{\lambda}\hat{k}$ is the wave vector, n refractive index of the surrounding environment, and $\boldsymbol{R}_{12}$ a spatial vector defining the direction and size of the intermediate space between the dipoles.

From (2.3) we observe that the radiation intensity depends on the direction of light propagation. Moreover one can in principle expect a strong contrast between light emitted in opposite directions along the dimer axis, that is $(\pm\boldsymbol{k})$ directions. The ratio of scattered intensities along these opposite directions may then be determined from (2.3) as

$$R_{12} = \frac{1 + f(R_p)\cos(kL + \Delta\varphi_{12})}{1 + f(R_p)\cos(-kL + \Delta\varphi_{12})} \quad (2.4)$$

For simplification reasons, we put $f(R_p) = \frac{2R_p}{1+R_p^2}$ and $R_p = \frac{|\boldsymbol{p}_2|}{|\boldsymbol{p}_1|}$. From (2.4) it is straightforward to conclude that the ratio of left/right-scattered intensities is

maximized in a situation corresponding to $|\boldsymbol{p}_1| = |\boldsymbol{p}_2|$, $\Delta\varphi_{12} = -\frac{\pi}{2}$ and $L = \frac{\lambda}{4n}$. So for a certain wavelength when all these conditions are fulfilled, perfect constructive/destructive far-field interference will occur in opposite directions along the dimer axis. The resulting radiation pattern of such a situation is graphically depicted in Figure 2.2.

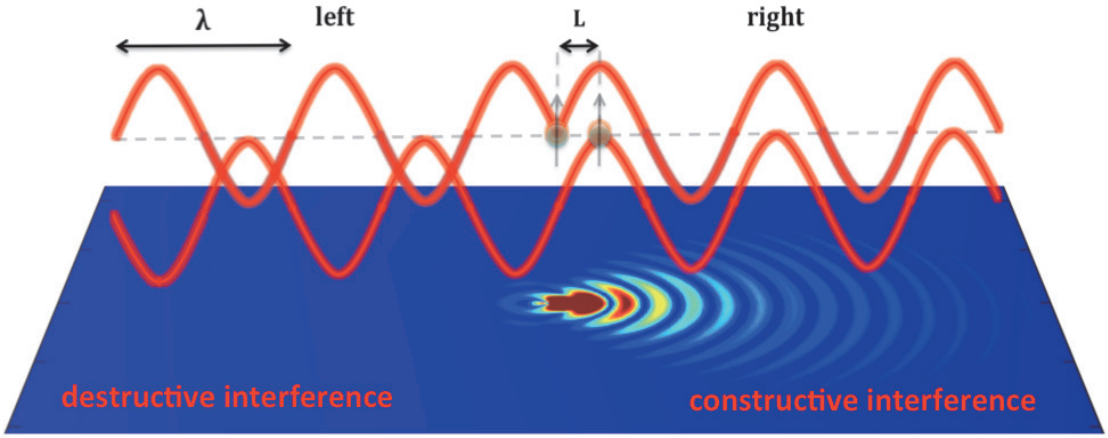

Figure 2.2: *Schematic illustration of the net radiation pattern from a pair of detuned dipole emitters when conditions for total constructive/destructive interference are fulfilled. The upper rays illustrate the radiation from an individual dipole emitter while the lower plane shows the resulting interference pattern in opposite directions along the dimer axis.*

Chapter 3

Optical Resonances in Metallic Nanoparticles, Quantum Dots and Molecules

In this chapter, several intriguing results of light-matter interactions at the nanoscale are presented and described. It turns out that the intuitive properties possessed by noble metals (Au, Ag etc.) are drastically altered when considering small distinct entities with nanoscale dimensions. This is also true for tiny entities of semiconducting crystals (quantum dots). Much of these properties originate from spatial confinement of electrons. These phenomena and several further implications of those are systematically described within Sections 3.1-3.4.

3.1 Optical properties of metallic nanoparticles

In nanoscale metallic entities the surface electrons are spatially confined to a region much shorter than the wavelength of electromagnetic fields with frequencies in the THz regime. In the presence of an oscillating incident field, an overall displacement of the surface electrons will therefore transpire. This, in turn gives rise to a restoring force due to the charge separation between the displaced electron cloud and positively charged lattice. These forces will then result in coherent periodic oscillations of surface charge densities, which are greatly enhanced at specific wavelengths depending on the particle geometry and material. This phenomenon is entitled *localized surface plasmon resonances* (abbreviated *LSPR*) [8], and will be theoretically derived within this section.

According to Maxwell's equations in frequency space, the electric displacement field in a medium with dielectric function $\varepsilon(\boldsymbol{k}, \omega)$ can be expressed as

$$\mathbf{D}(\mathbf{k}, \omega) = \varepsilon_0 \varepsilon(\mathbf{k}, \omega)\mathbf{E}(\mathbf{k}, \omega) = \varepsilon_0 \mathbf{E}(\mathbf{k}, \omega) + \mathbf{P}(\mathbf{k}, \omega) \tag{3.1}$$

where ε_0, $\boldsymbol{E}(\boldsymbol{k}, \omega)$ and $\boldsymbol{P}(\boldsymbol{k}, \omega)$ are the vacuum permittivity, electric field vector and polarizability vector respectively [9]. The time-dependent displacement field can furthermore be expressed as

$$\mathbf{D}(\mathbf{R}, \mathrm{t}) = \varepsilon_0 \int_{-\infty}^{\infty} \int_{-\infty}^{\infty} \varepsilon(\mathbf{R} - \mathbf{R_0}, \mathrm{t} - \mathrm{t}_0)\mathbf{E}(\mathbf{R_0}, \mathrm{t}_0)\, \mathrm{d}\mathbf{R}_0 \mathrm{d}\mathrm{t}_0 \tag{3.2}$$

This is simply a convolution of the dielectric function and electric field [26], which entail that the displacement field in space and time domain at point $(\boldsymbol{R}, t)$ depends on every other spatial points $\boldsymbol{R}_0$ and all previous times t_0, which indicates that (3.2) reflects causality in dynamics of electromagnetism.

The equation of motion for a single conduction electron can further be denoted, according to Drude-Sommerfeld theory in the time domain, as

$$\mathrm{m}\frac{\partial^2 \mathbf{r}}{\partial \mathrm{t}^2} + \mathrm{m}\gamma \frac{\partial \mathbf{r}}{\partial \mathrm{t}} = -\mathrm{e}\mathbf{E}(\mathrm{t}) \tag{3.3}$$

where m, γ, e and $\boldsymbol{r}(t)$ are electron mass, damping parameter, elementary charge and spatial displacement vector respectively. By applying a Fourier transform to the differential equation (3.3), the resulting expression for the frequency dependent equilibrium displacement vector yields

$$\mathbf{r}(\omega) = \frac{{}^{\mathrm{e}}/_{\mathrm{m}}}{\omega^2 + i\gamma\omega}\mathbf{E}(\omega) \tag{3.4}$$

Here the parameter i denotes the imaginary unit. The macroscopic polarizability vector may further be interpreted as the number of dipole moments per unit volume, and it is therefore suitable to write such a quantity according to $\boldsymbol{P}(\omega) = -n_e e\boldsymbol{r}(\omega)$, where n_e represent the electron density in the metal. By combining (3.1) and (3.4) the resulting form of the metal dielectric function can be written as [8]

$$\varepsilon(\omega) = 1 - \frac{\omega_p^2}{\omega^2 + i\gamma\omega} \tag{3.5}$$

$$\omega_p = \sqrt{\frac{n_e}{\varepsilon_0 m}}e \tag{3.6}$$

where ω_p describes the plasma frequency of the metal. The derivation is proceeded by applying the so-called *quasi-static (Rayleigh) approximation*, which is suitable when electrons are confined to a spatial region much shorter than the wavelength of the incident field.

Finally, it is possible to obtain a net polarizability function for spheroidal shaped metallic nanoparticles according to [9]

$$\alpha_{x,y,z}(\omega) = V\frac{\varepsilon(\omega) - \varepsilon_d}{\varepsilon_d + L_{x,y,z}[\varepsilon(\omega) - \varepsilon_d]} \tag{3.7}$$

Parameters V, $L_{x,y,z}$, and ε_d are the volume, geometrical form factor in the x, y or z direction which depends exclusively on aspect ratio, and dielectric constant of the surrounding medium respectively. This derivation of the polarizability function does not account for so-called *radiation damping* and *dynamic depolarization*. Radiation damping occur as supression of the dipole moment, and hence lower magnitude in resonance enhancements, due to radiative losses in larger nanoparticles. Dynamic depolarization accounts for enhancement maximum in nanoparticles with small but finite volumes, as well as a spectral resonance shifts when the volume of the nanoparticles are increased [27]. These factors must be paid attention to in order to get a more accurate theoretical estimation for the resonance position and overall spectral features when studying light scattered from metallic nanoparticles.

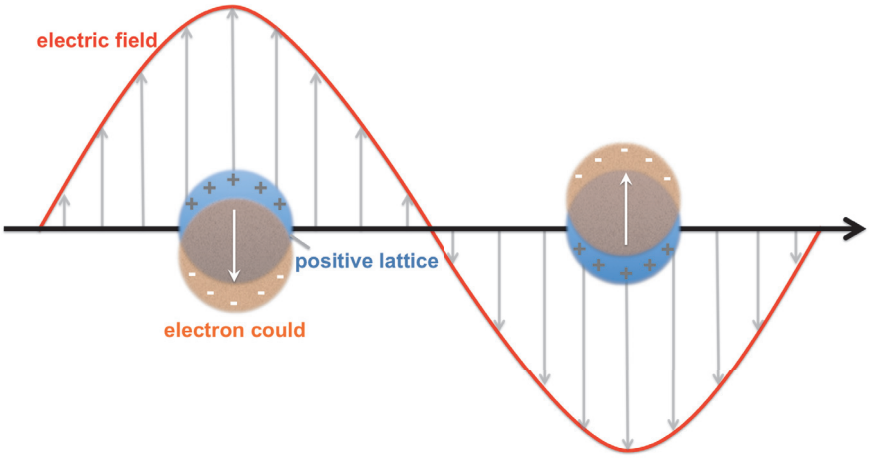

Figure 3.1: *Illustration of the localized surface plasmon resonance phenomenon. The whole electron cloud is displaced with respect to the positively charged lattice, and will oscillate back and forth until it finally reaches its equilibrium.*

In order to account for these phenomena a suited tactic is to go beyond the quasi-static approach and instead utilize the *modified long-wavelength approximation MLWA* [28]. The polarizability function in (3.7) is then altered according to

$$\alpha_{MLWA}(\omega) = \frac{\alpha_{x,y,z}(\omega)}{4\pi - \frac{k^2}{r_n}\alpha_{x,y,z}(\omega) - i\frac{2}{3}k^3\alpha_{x,y,z}(\omega)} \tag{3.8}$$

where $r_n \in \{r_x, r_y, r_z\}$. The second term in the denominator accounts for the appearance of an enhancement maximum for particles with small finite volumes. The third term reflects radiation-damping which give rise to dissipation and hence both broadens and decrease the magnitude of the spectral resonance peak for larger nanoparticle volumes.

Eventually, the resulting scattering- and extinction cross sections can be deduced in pursuance with the expressions [9]

$$\sigma_{sca}(\omega) = \frac{\omega^4 n^4}{6\pi c^4}|\alpha(\omega)|^2 \tag{3.9}$$

$$\sigma_{ext}(\omega) = \frac{\omega n}{c} Im\{\alpha(\omega)\} \tag{3.10}$$

Parameters n and c denotes the refractive index of the surrounding medium and the vacuum speed of light respectively. The absorbtion cross section is consequently calculated as the result $\sigma_{abs}(\omega) = \sigma_{ext}(\omega) - \sigma_{sca}(\omega)$. These functions are maximized at a specific *localized surface plasmon resonance frequency* according to

$$\omega_{\text{LSPR}} = \frac{\omega_p}{\sqrt{1 + \left({}^{1}/_{L_{x,y,z}} - 1\right) n^2}} \tag{3.11}$$

The displacement of surface charge density related to localized surface plasmon resonances is illustrated in Figure 3.1. From (3.11) we further see that the resonance wavelength shifts approximately linearly with refractive index of the surrounding environment, which is simulated in Figure 3.2.

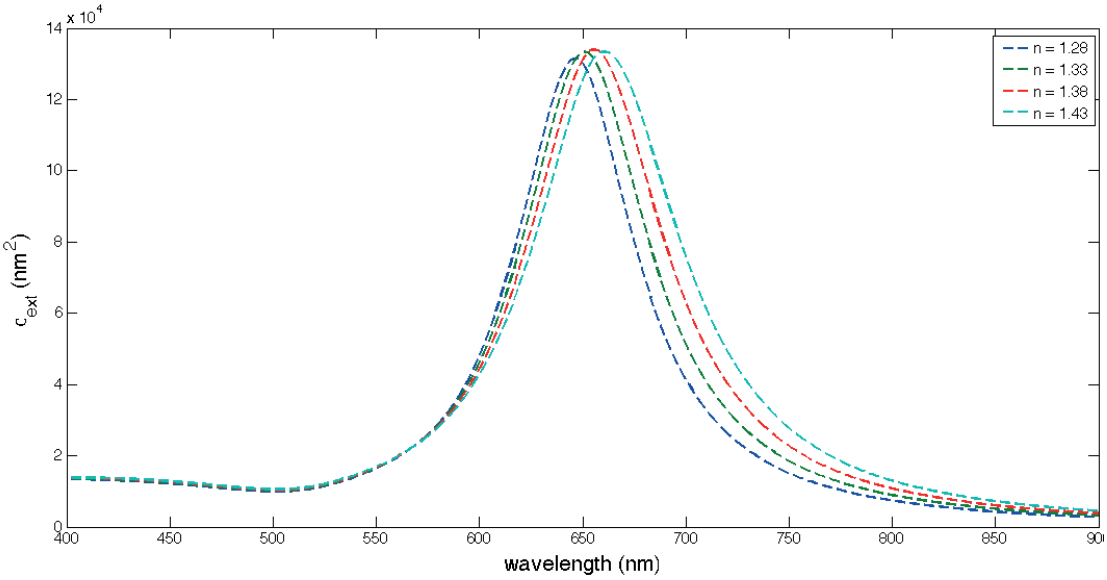

Figure 3.2: *Graph illustrating how the plasmonic extinction spectrum red-shifts when the refractive index of the surrounding environment is increased. By quantifying the amount of nanometer peak shift when the refractive index is altered, it is possible to deduce a sensitivity value and the plasmonic structure may be used as a molecular sensor.*

3.1.1 Radiating dipole located near a planar dielectric interface

As previously stated, the polarizability function in (3.8) reaches a maximum value when the wavelength of the incident light corresponds to that of ω_{LSPR} for a certain nanodisk. This entail that the plasmonic particle will radiate a lot of light in directions both left and right perpendicular to the axis along which the charge density oscillates. An interesting aspect of scattering from nanoscale objects takes place when they are positioned close to a plane dielectric interface. This can be modeled by considering oscillating electric dipoles located near a plane surface. A unique radiation pattern arises due to properties of evanescent fields [29]. Via the following steps one can explicitly derive an expression for the radiation pattern to understand the scattering dynamics when plasmonic nanoparticles are positioned on top of plane optically thick dielectric media.

Starting by expressing the time averaged energy-flux Poynting vector as $\langle \boldsymbol{S} \rangle = \frac{1}{2} Re\{\boldsymbol{E} \times \boldsymbol{H}^*\}$, where the asterisk denotes the complex conjugate of the frequency dependent magnetic field vector [8]. By furthermore exploiting the relation between electric and magnetic field in the far-zone as $\hat{n}_k \times \boldsymbol{E} = v\boldsymbol{B} \Longrightarrow \boldsymbol{H} = v^{-1}\mu^{-1}\boldsymbol{E}$, it is straight forward to show that the far-field expression for the time-averaged Poynting

vector may be expressed according to

$$\langle \boldsymbol{S} \rangle_{far} = \frac{1}{2}\sqrt{\frac{\varepsilon_0 \varepsilon}{\mu_0 \mu}}|\boldsymbol{E}|^2 \hat{n}_k \tag{3.12}$$

The parameter $\hat{n}_k = \frac{\boldsymbol{k}}{|\boldsymbol{k}|}$ is a unit vector in the radial direction away from the dipole and $\varepsilon_0, \mu_0, \varepsilon$ and μ are the vacuum permittivity, vacuum magnetic susceptibility, relative dielectric function and magnetic susceptibility of the lower medium respectively. The radiated power per unit solid angle, a radial distance *R* away from the dipole source, is thus written as

$$P = p(\Omega)d\Omega = R^2 \langle \boldsymbol{S} \rangle_{far} \cdot \hat{n}_k \tag{3.13}$$

By moreover assigning a dipole moment $\boldsymbol{\mu} = (\mu_x, \mu_y, \mu_z)$ to the oscillating charge density, the resulting electric field in the far-zone may further be expressed according to [8]

$$\boldsymbol{E} = \begin{bmatrix} E_\theta \\ E_\phi \end{bmatrix} = \frac{k_u^2}{4\pi\varepsilon_0\varepsilon_u}\frac{e^{ik_g R}}{R}\begin{bmatrix} [\mu_x \cos\phi + \mu_y \sin\phi]\cos\theta \boldsymbol{\Phi}_2^{(2)} - \mu_z \sin\theta \boldsymbol{\Phi}_2^{(1)} \\ -[\mu_x \sin\phi + \mu_y \cos\phi]\boldsymbol{\Phi}_2^{(3)} \end{bmatrix} \tag{3.14}$$

$$\boldsymbol{\Phi}_2^{(1)} = \frac{n_g \cos\theta}{n_u\sqrt{(n_u/n_g)^2 - \sin^2\theta}} t_p(\theta) e^{ik_g h\sqrt{(n_u/n_g)^2 - \sin^2\theta}} \tag{3.15}$$

$$\boldsymbol{\Phi}_2^{(2)} = -\frac{n_g}{n_u} t_p(\theta) e^{ik_g h\sqrt{(n_u/n_g)^2 - \sin^2\theta}} \tag{3.16}$$

$$\boldsymbol{\Phi}_2^{(3)} = \frac{\cos\theta}{\sqrt{(n_u/n_g)^2 - \sin^2\theta}} t_s(\theta) e^{ik_g h\sqrt{(n_u/n_g)^2 - \sin^2\theta}} \tag{3.17}$$

where $n_{u,g}$ describes the refractive index of the upper and lower medium respectively, $k_{u,g} = \frac{2\pi}{\lambda} n_{u,g}$ the wave vector magnitude, and *h* represents the distance which the oscillating dipole is located above the plane dielectric interface. The functions $t_{p,s}(\theta)$ are Fresnel amplitude coefficients for p- and s-polarized light respectively. The resulting radiated power per solid angle can then be calculated by a combination of (3.13) together with (3.14) and (3.15-3.17).

By then studying the angular dependence of the resulting function, one find that if the dipole is positioned close enough ($\lambda/100 < h < \lambda/10$) to the plane glass surface, a significant portion of the radiation pattern will be concentrated in the so-called *forbidden zone*. The term *forbidden* relates to the fact that the nature of the fields originating from the radiating dipoles located very close to the interface are evanescent, but may be transformed into propagating modes below the interface due to refractive index mismatch between the upper and lower medium. The direction for such a transformed propagating wave always occur at an angle equal or greater than the critical $\theta_c = \arcsin(n_u/n_g)$ with respect to the normal to the lower-upper

medium interface. Hence this light can be regarded as *forbidden* in ordinary terms of scattering due to the fact that evanescent fields from dipoles located further away from the plane interface will decay off before it ever reaches the interface. Therefore the scattered light from these sources will end up in the *allowed zone* ($\theta < \theta_c$) inside the dielectric medium.

The radiation pattern from dipoles located a distance h above a plane dielectric interface is illustrated in Figure 3.3. The region above/below the dotted lines, in the lower medium, corresponds to the forbidden/allowed zone respectively. Notice that the amount of light scattered into the forbidden zone decreases immensely when the height of the dipole location over the plane interface h increases, whereas the amount of light scattered into the allowed zone is independent of h.

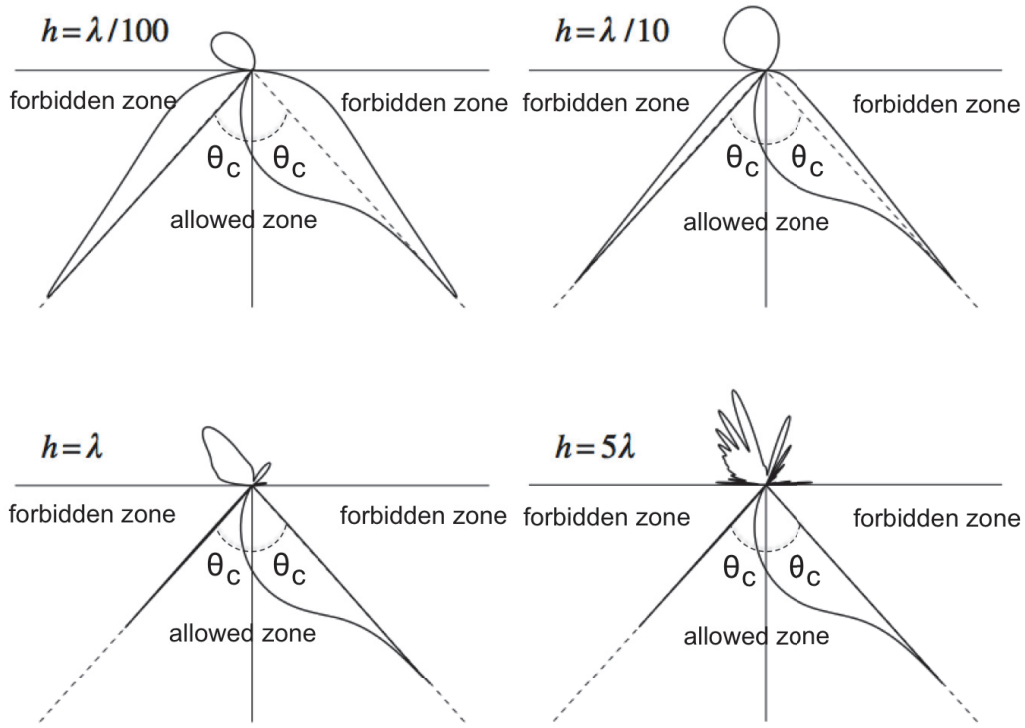

Figure 3.3: *Schematic drawing of how the amount of light radiated into the forbidden zone changes when the distance between the dipole emitter and the plane dielectric interface is altered. Note that the amount of light radiated in to the allowed zone is independent of the distance between the dielectric interface and dipole. Picture taken from [8].*

3.2 Delocalized electrons and optical resonances in molecules

Polyatomic molecules consist of microscopic structures where electrons, in many cases, are not specifically localized at a single atomic nucleus but instead have the ability to spatially move between several adjacent atoms. Molecular electrons with such properties are generally referred to as being *delocalized*. In quantum chemistry, the most frequent mathematical model to describe dynamics and additional properties of delocalized molecular electrons is by applying the concept of *molecular orbitals*

[30]. In this model, the probabilistic nature of a delocalized electron within the molecule is utilized and further described by wavefunctions according to

$$\psi_n(r,\theta,\phi) = \sum_{l,m} R_{nl}(r) Y_{lm}(\theta,\phi) \tag{3.18}$$

where index n relates to the orbital number. $R_{nl}(r)$ and $Y_{lm}(\theta,\phi)$ are radial hydrogen-like functions and spherical harmonics respectively. In order to relate obritals, such as described in (3.18), to interpret probabilistic outcomes one requires that every orbital should be normalized, i.e. [30]

$$\int_{r=0}^{\infty}\int_{\theta=0}^{\pi}\int_{\phi=0}^{2\pi} |\psi_n(r,\theta,\phi)|^2 r^2 \sin\theta \, dr d\theta d\phi = 1 \tag{3.19}$$

The knowledge of such a wavefunction makes it possible to extract the probability for a molecular electron to occupy a certain quantum state with a certain energy.

The energy relaxation between an excited state to a lower lying state is often possible through a release in energy through an emitted photon via so-called *spontaneous emission*. Spontaneous emission is possible due to coupling between the excited quantum state and vacuum quantum fluctuations [30]. The angular frequency of a photon emitted from a system with atomic energy levels E_1 and E_2 corresponds to $\omega_{12} = \frac{|E_2 - E_1|}{\hbar}$, see Figure 3.4.

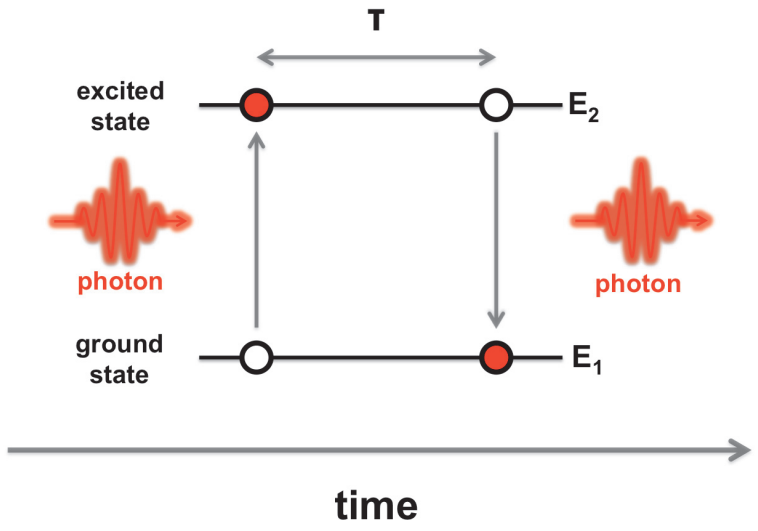

Figure 3.4: *Schematic drawing of the light-matter interaction process. A photon is absorbed by the molecular electrons and the system enters an excited quantum state for a time period τ before it relaxes to its energetic ground state through the emission of a photon. This photon energy corresponds to the energy difference between the excited and ground quantum state.*

From a quantum mechanical perspective, this result is obtained rather easily by solving the time-dependent Schrödinger equation which rely on Hermitian operators and does not take into account any energy dissipation or interaction with the surrounding environment [30].

However, in reality it is well documented that every atomic energy level, except the lowest lying ground state, experience a finite lifetime τ due to factors like Heisenbergs uncertainty principle

$$\Delta r \Delta p \geq \frac{\hbar}{2} \Leftrightarrow \Delta E \Delta t \geq \frac{\hbar}{2} \tag{3.20}$$

and further perturbations from the surrounding environment [31]. In (3.20) the following parameters $\Delta r, \Delta p, \Delta E, \Delta t$ are uncertainty in position, linear momentum, energy and time respectively.

In order to model the consequences of dissipation, it is possible to modify the Schrödinger equation for the excited quantum system to reflect field-coupling [30]

$$i\hbar \frac{\partial}{\partial t} \psi(\boldsymbol{r}, t) = \left(E - i\hbar \frac{\gamma}{2}\right) \psi(\boldsymbol{r}, t) \tag{3.21}$$

where $\gamma = 1/\tau$ and τ the lifetime of the quantum state. This implies that the wavefunction $\psi(\boldsymbol{r}, t)$ does not represent a quantum state with a well-defined real energy. By summing over all possible final states and taking the density of states in to account, each state-relaxation is assigned to a spectral distribution with a linewidth symmetrically spread around the resonance frequency.

From this proceedure, the intensity distribution of the excited quantum state will be proportional to a *Lorentzian function* of the form

$$f_{12}(\omega) = \frac{\gamma^2/4}{(\omega - \omega_{12})^2 + \gamma^2/4} \tag{3.22}$$

where the damping frequency parameter $\gamma = \gamma_{rad} + \gamma_{nr}$ depends on both radiative and non-radiative processes which accounts for energy dissipation in the system. It is hence self-evident that a maximum occur at the spectral position ω_{12} which is the optical *resonance frequency* [30].

Moreover, at frequencies $\omega = \omega_{12} \pm \frac{\gamma}{2} \Longrightarrow \Delta\omega = \omega_+ - \omega_- = \gamma$ the spectral function reaches its half-maximum value. The expression of (3.22) in the time domain [26]

$$f_{12}(t) = \frac{\gamma}{4} e^{-\frac{\gamma}{2}|t|} e^{i\omega_{12}t} \tag{3.23}$$

indicates that the dynamics of optical molecular excitations resembles that of a damped harmonic oscillator. The lifetime of the excited quantum state is hence explicitly related to the damping parameter according to $\tau = 2\gamma^{-1}$ since the magnitude of $f_{12}(t)$ becomes negligible for times $t > \tau$.

3.3 Quantum confinement and excitons in semiconducting crystals

Since both electrons and holes, in nanoscale semiconducting crystals, are restricted to move in small spatial dimensions the effects of *quantum confinement* becomes noticeable. One may treat an electronic excitation in the semiconducting crystal as a quasiparticle generally referred to as an *exciton*. In other words, the exciton is comprised by a bound electron-hole pair which is coupled together via attractive Coulomb interaction. The total Hamiltonian for the exciton is hence written as [8]

$$\widehat{H}_{exciton} = \underbrace{-\frac{\hbar^2}{2m_h}\boldsymbol{\nabla}_h^2}_{\substack{hole\\ kinetic\\ energy}} \underbrace{-\frac{\hbar^2}{2m_e}\boldsymbol{\nabla}_e^2}_{\substack{electron\\ kinetic\\ energy}} \underbrace{-\frac{e^2}{4\pi\varepsilon_0\varepsilon_s|\boldsymbol{R}_h - \boldsymbol{R}_e|}}_{\substack{electron-hole\\ Coloumb\\ interaction}} \tag{3.24}$$

Here m_h, m_e and ε_s describes the effective band masses of the hole, electron in the exciton and dielectric constant of the nanosized semiconductor respectively.

The term representing the electron-hole Coloumb interaction doesn't need to be taken into account when studying small semiconducting quantum dots, since the exciton is spatially confined to a very restricted region [8]. Hence, both hole and electron may be treated theoretically as a *particle-in-a-box* which, by solving the time-independent Schrödinger equation, results in discretized energy levels according to [31]

$$E_{e,h} = \frac{\hbar^2\pi^2}{2m_{e,h}}\left[\left(\frac{n_x}{L_x}\right)^2 + \left(\frac{n_y}{L_y}\right)^2 + \left(\frac{n_z}{L_z}\right)^2\right] \tag{3.25}$$

The box volume is described by $V = L_xL_yL_z$ and the different energy levels are determined by parameters $\{n_x, n_y, n_z\} \in \mathbb{N}$. Hence, according to (3.25), the smaller the side lengths of the box, the higher the energies. This phenomenon is a consequence of Heisenbergs uncertainty principle which states that the uncertainty in exciton linear momentum increases (hence also uncertainty in its kinetic energy) when restricted to a more well defined spatial region [8]. By exploiting the *effective mass approximation* model [32], one may furthermore derive the shift of band-gap energy ΔE_{bg} due to exciton confinement according to the expression

$$\Delta E_{bg} = \frac{\hbar^2\pi^2}{2\mu R^2} - \frac{1.8e^2}{\varepsilon R} \tag{3.26}$$

where μ is the reduced mass of the electron-hole pair and R the radius of the quantum dot. An additional factor to notice is that the non-radiative decay increases with size of the quantum dot [33]. Due to this, small quantum dots have rather high quantum efficiencies for radiative decay and are hence considered to be very suitable for optoelectronic applications at the nanoscale [8].

3.4 Resonant and non-resonant plasmon-exciton coupling

If the circumstances are right, it is possible for plasmonic modes to interact with optical excitations in molecules and/or semiconducting nanocrystals (quantum dots).

These type of interaction are often divided into *non-resonant* and *resonant* coupling depending on the spectral overlap between the plasmon-exciton modes. In the non-resonant case the spectral overlap between the exciton and plasmon is negligible and the molecules/quantum dots may be regarded as a non-absorbing dielectric medium around the plasmonic particle which results in a shift in plasmon resonance in a manner described by expression (3.11). This phenomenon is fundamental for plasmonic sensing schemes described in the upcoming subsection 3.4.1. Resonant coupling is a substantial part within this thesis, therefore it is described in more detail in a separate chapter (Chapter 4). This is done in order to deduce and illustrate the underlying theory *strong coupling* and formation of *hybrid states* in sufficient detail.

3.4.1 Plasmonics for refractive index sensing

Plasmonic nanoparticles show great potential in acting as future sensors within a wide range of industrial fields. Due to properties as its spatial nanoscale dimensions and sensitivity to local environmental dielectric alterations, plasmonic nanoparticles show very promising applications in both material industries and biomedical science [34-38]. The fundamental approach to exploit nanoscale plasmonic particles as sensors is briefly described within this section.

As described earlier in this thesis, surface plasmons are highly sensitive to dielectric changes in their local environment. How sensitive a certain plasmonic nanoparticle is to ambient environmental changes depends on several factors like geometry and material composition, but also the ease of electron polarization in the nanoparticle.

In the field of plasmonic sensing one often distinguishes between *bulk-sensing* and *local sensing*. In the bulk sensing model one assumes that the total ambient environment, in which the nanoparticles are located, is replaced by a medium with different dielectric properties. In local sensing it is assumed that the dielectric properties changes only within a region of the probe volume around the nanoparticle. By assigning the spatial range of the probing region with a parameter d_p one clearly sees that the local sensing model converges to the bulk sensing model when $d_p \to \infty$. The simplest way of determining the plasmonic signals in these two sensing platforms are done in the bulk model [12].

To quantify how sensitive a certain model is to dielectric changes of the ambient environment it is convenient to define a sensitivity parameter, simply defined as $\frac{\partial \lambda_{LSPR}}{\partial n}$ where λ_{LSPR} is the LSPR wavelength and n the refractive index of the surrounding medium. This means that the sensitivity aspect describes the change in resonance wavelength for a unit change in the refractive index of the ambient medium. Further analytical investigation shows that the sensitivity of a sub-wavelength nano-antenna can be written as [12]

$$\frac{\partial \lambda_{LSPR}}{\partial n} = \frac{2Re\{\varepsilon(\lambda)\}}{n}\left(\frac{\partial Re\{\varepsilon(\lambda)\}}{\partial \lambda}\right)^{-1}\Bigg|_{\lambda=\lambda_{LSPR}} \tag{3.27}$$

Here $\varepsilon(\lambda)$ is the wavelength dependent complex valued dielectric function described within the previous chapters.

Chapter 4

Interactions between a Resonant Cavity and Quantum Emitters

A model widely used to simulate the quantum nature of light-matter interactions is a two-level system positioned inside a resonating cavity [39]. This scheme predicts several experimental outcomes in modern quantum optics and is regarded as a cornerstone in our understanding of this field. Hence, it is one of the most prominent tools to forecast intriguing dynamics of quantum states. The following chapter present ulterior theoretical foundations and derivations to obtain a fundamental base for light-matter interactions at the quantum level.

4.1 Theoretical background of cavity-emitter interactions

The interaction between a quantum emitter (atom, molecule, quantum dot etc.) and spatially confined field can be initially understood by studying an atomic electron in the presence of a quantized non-relativistic external electromagnetic field [39]. The resulting Hamiltonian for such a system is written according to

$$\widehat{H} = \frac{\left[\widehat{\boldsymbol{p}} + e\widehat{\mathbf{A}}(r,t)\right]^2}{2m} - e\phi(r,t) + V(r) \tag{4.1}$$

where $\widehat{\boldsymbol{p}} = -i\hbar\boldsymbol{\nabla}$, $\widehat{\mathbf{A}}(r,t)$, $\phi(r,t)$ and $V(r)$ are linear momentum operator, field vector potential, field scalar potential and the atomic nucleus electron energy potential. By furthermore applying gauge invariance and selecting the so-called *Coloumb gauge* ($\boldsymbol{\nabla}\cdot\widehat{\mathbf{A}}(r,t) = 0$) together with exploiting the *dipole-approximation* ($\widehat{\mathbf{A}}(r,t) \approx \widehat{\mathbf{A}}(t)$), the Hamiltonian may be rewritten as

$$\widehat{H} = \frac{\widehat{\boldsymbol{p}}^2}{2m} + V(r) - \widehat{\boldsymbol{\mu}}\cdot\widehat{\boldsymbol{E}} \tag{4.2}$$

where parameter $\hat{\mu} = e\hat{r}$ is the transition dipole moment operator for the quantum emitter. The last term in the expression describes interaction between the electron and the external electric field. By finally utilizing a general expression for a quantized electric field inside a cavity, together with the *rotating wave approximation (RWA)* [40], the Hamiltonian can at last be defined as

$$\widehat{H} = \widehat{H}_0 + \hbar g(\widehat{\boldsymbol{a}}\hat{\sigma}_+ + \widehat{\boldsymbol{a}}^\dagger\hat{\sigma}_-) \tag{4.3}$$

This is generally referred to as the *Jaynes-Cummings Hamiltonian* [41]. The first term relates to the intrinsic energy of both electron and cavity-field, and the second term corresponds to the interaction energy. The different interaction parameters within (4.3) are further specifically expressed as

$$g = \mu \underbrace{\sqrt{\frac{\hbar\omega}{2\varepsilon_0 \varepsilon V_m}}}_{=|E_{vac}|} = \frac{\mu}{n}\sqrt{\frac{hc}{2\varepsilon_0 \lambda V_m}}$$

$$\hat{a} = \frac{\omega\hat{q} + i\hat{p}}{\sqrt{2\hbar\omega}}\,, \hat{a}^{\dagger} = \frac{\omega\hat{q} - i\hat{p}}{\sqrt{2\hbar\omega}} \tag{4.4}$$

$$\hat{\sigma}_{+} = \left|N_{pl} + 1\,, g\right\rangle\left\langle N_{pl}\,, e\right|\,, \hat{\sigma}_{-} = \left|N_{pl}\,, e\right\rangle\left\langle N_{pl} + 1\,, g\right|$$

$$\boldsymbol{g} = coupling\ strength\ between\ cavity\ and\ emitter$$
$$\boldsymbol{\mu} = transition\ dipole\ moment\ of\ emitter$$
$$\boldsymbol{V_m} = cavity\ mode\ volume$$
$$\boldsymbol{E_{vac}} = vacuum\ electric\ field$$
$$\hat{\boldsymbol{a}} = cavity\ field\ quantum\ annihilation\ operator$$
$$\hat{\boldsymbol{a}}^{\dagger} = cavity\ field\ quantum\ creation\ operator$$
$$\hat{\boldsymbol{\sigma}}_{+} = emitter - cavity\ energy\ transfer\ operator$$
$$\hat{\boldsymbol{\sigma}}_{-} = cavity - emitter\ energy\ transfer\ operator$$
$$\left|\boldsymbol{N_{pl}} + \boldsymbol{1}\,, \boldsymbol{g}\right\rangle = state\ with\ N_{pl} + 1\ cavity\ field\ quanta\ and\ no\ exciton$$
$$\left|\boldsymbol{N_{pl}}\,, \boldsymbol{e}\right\rangle = state\ with\ N_{pl}\ cavity\ field\ quanta\ and\ one\ exciton$$

Note that the ket-vectors $\left|N_{pl} + 1\,, g\right\rangle = \left|N_{pl} + 1\right\rangle \otimes |g\rangle$ and $\left|N_{pl}\,, e\right\rangle = \left|N_{pl}\right\rangle \otimes |e\rangle$ should be interpreted as the tensor product between the ket-states representing individual cavity-field modes and exciton states.

4.1.1 The notion of strong coupling and formation of hybrid states

When it comes to the fundamental understanding and theoretical description of the strong coupling phenomenon, there are plenty of different theoretical models which results in similar outcomes. For instance, many recent works have used a classical coupled-oscillator model to include resonance frequencies, dissipation and coupling rates, which yield spectral outcomes comparable to experimental observations [42-43]. This model works rather well to describe systems where plenty of quantum emitters coherently act as a single giant emitter coupled to the cavity resonance. However, this model mediates inadequate outcomes when modelling situations where a single or only a few quantum emitters are coupled to the resonating cavity. Under these circumstances a non-classical theoretical approach is needed since the quantum nature of molecules becomes evident when they are only a few in numbers.

In the case of near-field mediated coupling it is suitable to choose a model which describes how virtual particles tunnel back and forth between a resonating nanocavity and a two-level quantum emitter system. The Hamiltonian for such a system, with N_{pl} cavity excitations and a single quantum emitter, can be described according to [39]

$$\mathbf{H} = \hbar\omega_{pl}\hat{a}^{\dagger}\hat{a}\hat{\mathbb{I}} - \frac{\hbar\omega_0}{2}\sigma_z + \hbar g\{\hat{\boldsymbol{a}}\left|N_{pl} + 1\,, g\right\rangle\left\langle N_{pl}\,, e\right| + h.c.\} \tag{4.5}$$

where $\hat{\mathbb{I}}$ and σ_z refers to the identity matrix and Pauli matrix respectively. Note also that the term related to cavity zero-point energy has been removed, indicating a new common energy reference. The mode frequencies $\Omega_{\pm}$ are found by solving the eigenvalues to the time-dependent Schrödinger equation for the system and results in

$$\Omega_{\pm} = \omega_{pl}\left(N_{pl} + \frac{1}{2}\right) \pm \sqrt{g^2(N_{pl}+1) + \frac{\delta^2}{4}} \tag{4.6}$$

where $\delta = \omega_{pl} - \omega_0$ is the frequency detuning between cavity and emitter. To simplify this expression further we may limit ourselves to study the case where cavity and emitter resonance frequencies overlaps, i.e. $\delta = 0$ ($\omega_{pl} = \omega_0 \equiv \omega_R$), which gives

$$\widehat{\Omega}_{\pm} = \omega_R\left(N_{pl} + \frac{1}{2}\right) \pm g\sqrt{N_{pl}+1} \tag{4.7}$$

The corresponding eigenfunctions to the eigenvalues in equation (4.6) describes wavefunctions of so-called *dressed states* or *hybrid states*

$$\begin{aligned} |\psi_+\rangle &= \cos\theta\,|N_{pl}\,, e\rangle + \sin\theta|N_{pl}+1\,, g\rangle \\ |\psi_-\rangle &= \cos\theta|N_{pl}+1\,, g\rangle - \sin\theta\,|N_{pl}\,, e\rangle \end{aligned} \tag{4.8}$$

The parameter θ is further defined as

$$\theta = \frac{1}{2}\arctan\left(\frac{2g\sqrt{N_{pl}+1}}{\delta}\right) \tag{4.9}$$

Hence, it is straightforward to deduce the probabilities to find the system in states $|\psi_+\rangle$ and $|\psi_-\rangle$, with the emitter being initially excited/deexcited. The expressions for these probabilities yields

$$\begin{gathered} P_{+e} = \cos^2\theta\ , P_{-e} = \sin^2\theta \\ \text{and} \\ P_{+0} = \sin^2\theta\ , P_{-0} = \cos^2\theta \end{gathered} \tag{4.10}$$

In addition, an interesting situation is to study the case where the cavity and emitter resonances completely coincide, i.e. $\omega_{pl} \to \omega_0 \Rightarrow \delta \to 0$. From (4.9) it is evident that the resulting value of the parameter θ then becomes $\frac{\pi}{4}$, which indicates that both cavity and emitter wavefunctions are weighted equally. This entail that the excitation is delocalized evenly over both cavity and quantum emitter.

Note that this condition is fulfilled for any value of $g > 0$, but it is only when the overlap between the two hybridized modes is negligable $\left(g > [\gamma_{pl}, \gamma_0]\right)$ that the system is considered to be in a *strong coupling* state. In such a coupling regime, the rate which energy is transferred between the cavity and emitter overcomes any of the dissipation rates in the system. As a result, the probability for the excitation to be transferred back to the cavity after it has been absorbed and reemitted as a photon from the quantum emitter is sufficiently large. Hence the energy in the system may oscillate back and forth between the cavity and emitter several times before it escapes to the surrounding medium [8]. The situation corresponding to photons trapped inside

a resonating cavity, coupled to a two-level system, together with the resulting energy ladder are shown in Figure 4.1.

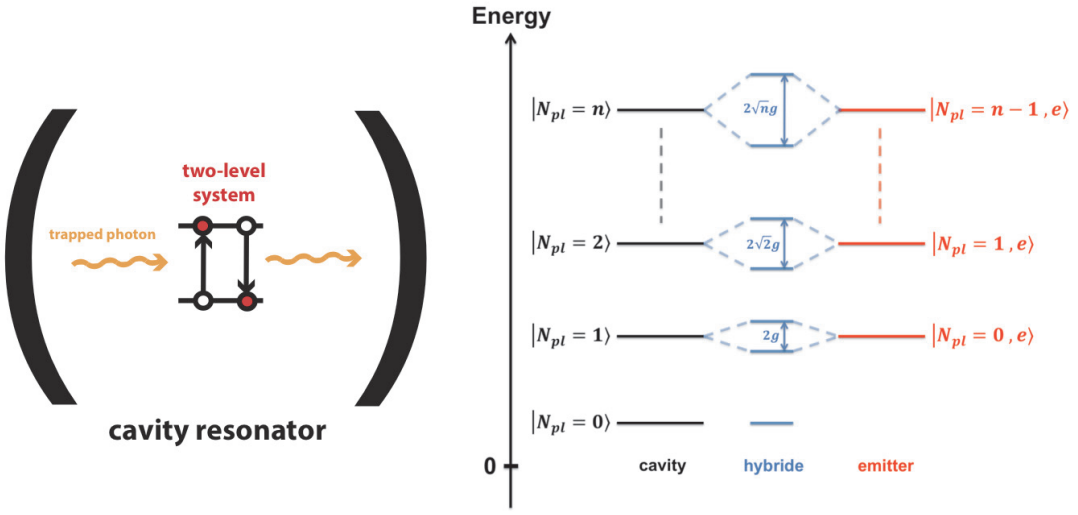

Figure 4.1: *(Left) Drawing of a quantum emitter (two-level system) placed inside a resonating cavity. (Right) The resulting energy ladder of both cavity and emitter as well as the formed hybrid modes (blue lines).*

The model derived so far does not account for any dissipation or dephasing since the Hamiltonian in (4.5) is exclusively described by Hermitian operators [31]. In order to account for both cavity and emitter energy dissipation it is possible to apply the so-called *Kossakowski-Lindblad* master equation [44] of the form

$$\frac{\partial \hat{\rho}}{\partial t} = \frac{i}{\hbar}[\hat{\rho}\,, \mathbf{H}] + \mathcal{L}_{cavity} + \mathcal{L}_{emitter}$$

$$\mathcal{L}_{cavity} = -\frac{\gamma_{pl}}{2}(\hat{\boldsymbol{a}}^{\dagger}\hat{\boldsymbol{a}}\hat{\rho} + \hat{\rho}\hat{\boldsymbol{a}}^{\dagger}\hat{\boldsymbol{a}} - 2\hat{\boldsymbol{a}}\hat{\rho}\hat{\boldsymbol{a}}^{\dagger}) \tag{4.11}$$

$$\mathcal{L}_{emitter} = -\frac{\gamma_0}{2}(\hat{\boldsymbol{\sigma}}_{+}\hat{\boldsymbol{\sigma}}_{-}\hat{\rho} + \hat{\rho}\hat{\boldsymbol{\sigma}}_{+}\hat{\boldsymbol{\sigma}}_{-} - 2\hat{\boldsymbol{\sigma}}_{-}\hat{\rho}\hat{\boldsymbol{\sigma}}_{+})$$

with

$$\hat{\rho} = \sum_{i=1}^{N} p_i |\psi_i\rangle\langle\psi_i| \tag{4.12}$$

Here $\hat{\rho}$ is the reduced density matrix of the system comprised by N different states. The probability for each state is denoted as p_i. A typical spectral feature of hybride states are shown in Figure 4.2 for several different values of the coupling strength between the cavity and emitter.

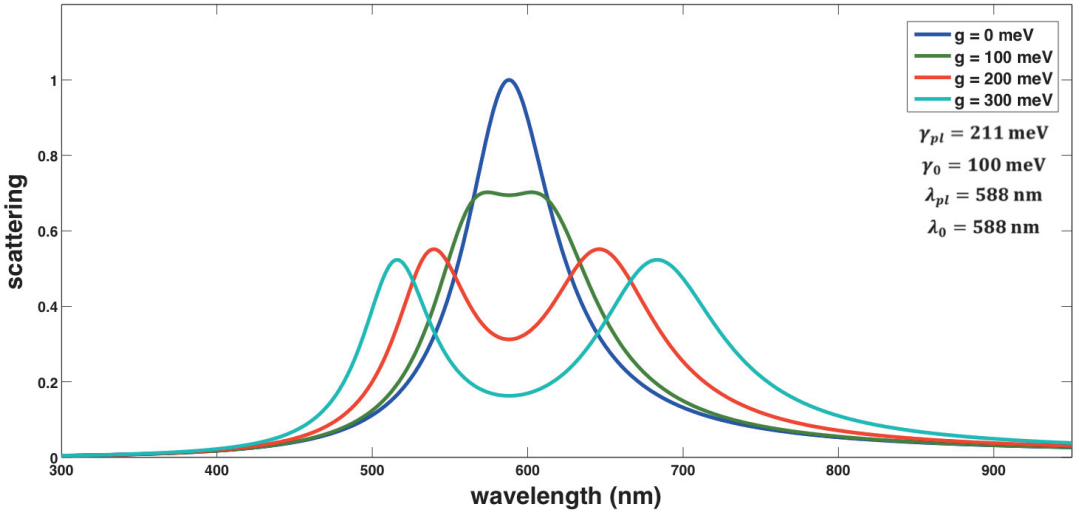

Figure 4.2: *Simulated scattering spectra displaying how the features changes from one Lorentzian shape to two distinct new hybrid modes when the coupling strength overcomes the dissipation rates of both cavity and emitter.*

4.1.2 The Dicke model: Interactions between a cavity and many emitters

The previously described model, which accounts for coupling between a resonating cavity and a two-level system, is only valid when the system contains a single quantum emitter. In reality, the case is often such that a massive amount of quantum emitters occupies the cavity mode volume, cooperatively interacting with a single cavity mode [45].

By recalling the Jaynes-Cummings Hamiltonian in expression (4.5), which is valid in the case of a single quantum emitter interacting with the cavity, one can revise certain aspects to make the Hamiltonian suitable for a single cavity mode which interacts coherently with N quantum emitters. The collective so-called *Dicke-operators* can then be expressed as

$$\widehat{D}_+ = \hat{b}^\dagger \left(N - \hat{b}^\dagger \hat{b}\right)^{1/2}$$
$$\widehat{D}_- = \left(N - \hat{b}^\dagger \hat{b}\right)^{1/2} \hat{b} \qquad (4.13)$$

and

$$\widehat{D}_z = \hat{b}^\dagger \hat{b} - \frac{N}{2}$$

where the operators $\hat{b}^\dagger$ and $\hat{b}$ are responsible for the creation and annihilation of the collective emitter quantum [45].

The eigenfunction notation for the ground state for the N quantum emitter case with N_{pl} cavity quanta, is then given by

$$|\psi_0\rangle = |0_1 0_2 0_3 \cdots\cdots 0_N\rangle \left|N_{pl} + 1\right\rangle \qquad (4.14)$$

and the collective coupling strength is furthermore denoted according to the expression

$$g_N = \sqrt{N}\mu|E_{vac}| \tag{4.15}$$

Note that the net coupling strength from N quantum emitters, coherently coupled to the cavity, my be written as $g_N = \sqrt{N}g_0$ which is just a factor of $\sqrt{N}$ greater than that of the case with a single quantum emitter, expressed in (4.4). Note that no dissipation rates are taken into account in this model, but can indeed be solved by assigning the previously described Kossakowski-Lindblad formalism.

4.1.3 Anticrossing in scattering versus absorption spectra

One of the most characteristic signatures for strongly interacting systems is anticrossing [17]. This entails that the spectral resonance positions of the two hybrid states never coincide, no matter what detuning the cavity-emitter system experiences. This phenomenon is depicted in Figure 4.3, where the energy of each hybrid mode (ω_+, ω_-) is plotted with respect to the cavity-emitter detuning.

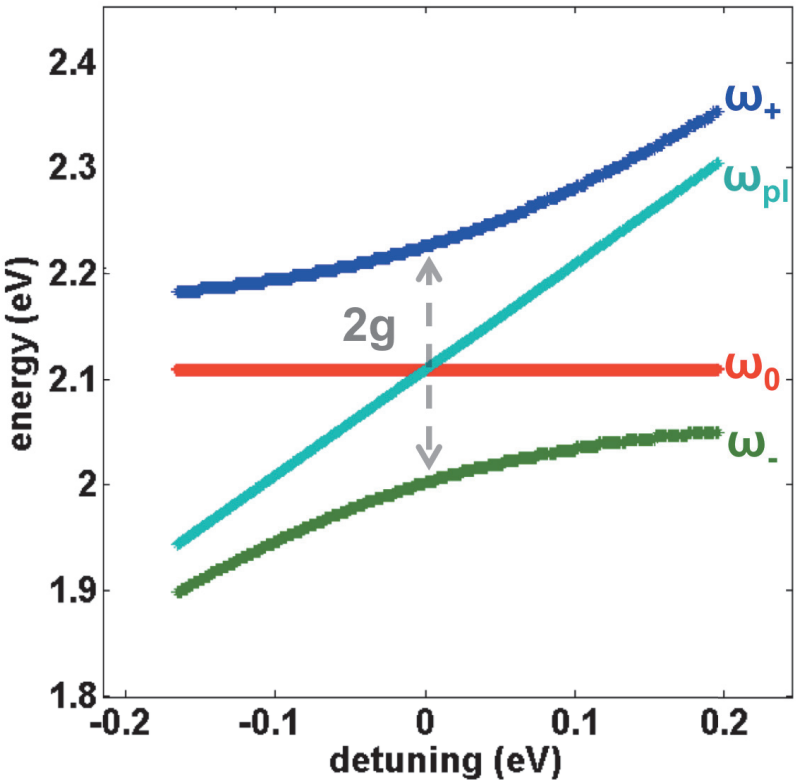

Figure 4.3: *Simulated values which indicates anti-crossing in scattering when to dipolar emitters are strongly coupled. The lines corresponds to upper/lower hybrid mode resonances (ω_+, ω_-) and cavity/emitter resonances (ω_{pl}, ω_0) and detuning is defined as $\delta = \omega_{pl} - \omega_0$.*

According to the scattering properties of the hybrid system, the Rabi energy splitting is equal to twice the coupling strength $2g$ at zero detuning. Note that the simulated

model is related to energy splitting in scattering spectra and not absorption or extinction.

It turns out that this information is insufficient in order to conclude whether a system is in a strong coupling regime or not. There are several possible phenomena which give rise to anti-crossing features in scattering, such as *surface enhanced absorption* and *electromagnetically induced ransparency (EIT)* [18]. In order to fully conclude what regime the system is operating in, one crucial property to investigate is if there is any simultaneous sign of anti-crossing in both scattering and absorption spectra.

Chapter 5

Experimental Methodology

This chapter describes experimental methods, optical setups, and various techniques that were utilized in order to perform and conduct measurements and extract knowledge of information in the realm of this thesis.

5.1 Coherent plasmon-plasmon interaction for directional emission

In order to realize a system with the ability to perform directional emission at the nanoscale, the concept of directional scattering presented in Chapter 2.2 was implemented. By moreover use the tunability of localized surface plasmon resonances in gold nanodisks, presented in Chapter 3.1, all conditions for simultaneous constructive/destructive interference in opposite directions along the dimer axis could be fulfilled.

5.1.1 Conceptual description of project idea

A final aim is to use nanoscale plasmonic structures to conduct a self-referenced sensing scheme by exploiting contrast from ratio of scattered intensities. A central issue with several present sensing schemes is that they require either microscopes or spectrometers that are both expensive and takes up valuable space [12]. These factors are limiting and impractical when considering a system aimed to work as a molecular-sensing device.

Inspiration was taken from several ideas presented in work done by both Evlyukhin *et al.* and Shegai *et al.* [46-48], which made use of directional scattering by asymmetric monometallic/bimetallic nanoscale dimers for acquiring high refractometric sensitivity. By studying the ratio of the scattered intensities for a monochromatic light source it is possible to reach enormously high directional scattering resonance sensitivity ξ_{DRS} by measuring the quantity

$$\xi_{DRS} \equiv \left.\frac{\partial R}{\partial n}\right|_{\lambda=const} \tag{5.1}$$

Note that the definition in (5.1) require that the changes in scattered intensity ratio are observed for an alteration of the refractive index at a constant wavelength, i.e. a single-wavelength sensing scheme [49].

Moreover, inspiration was taken from the theories described in Sections 2.2, 3.1 and 3.1.1 to realize nanoantennas in a dimer configuration which for a certain geometry and hence plasmon resonances detuning, give rise to directional emission in opposite directions along the dimer axis due to far-field interference. In addition these antennas could be positioned on top of an optically thick dielectric medium in order to extract light that originates from converted evanescent modes of the near-field from plasmonic resonances. As was described in Section 3.1.1, the angle of such propagating modes exceeds the critical angle of the lower/upper medium. Therefore detectors could be place at opposite directions along the dimer axis, at angles exceeding the critical and finally the intensity signal in each detector could be divided to form the ratio described in equation (2.4). Due to alterations in the ambient local

dielectric environment the conditions for constructive/destructive interferences change and result in an increase/decrease in ratio. Such system does have the potential to perform spectrometer-free, self-referenced, single-wavelength refractive molecular analysis in accordance to what is described by (5.1). Such a system moreover has the possibility to be constructed with cheap and ultra-compact components.

5.1.2 Asymmetric dimer sample fabrication

The samples, comprised by gold dimer disks, were fabricated using hole-mask colloidal lithography (HCL) [11]. By tilting the sample substrate with respect to the evaporation beam ($\pm 13.6°$) and by using different times of deposition, gold disks of different height (26 nm and 62 nm) were formed in a pairwise manner as dimer structures on top of the glass substrate, see Figure 5.1 (a). With a diameter around 100 nm the individual nanodisk in the dimer structure receive different aspect ratios and therefore supports localized plasmon resonances at distinct optical frequencies. The optimal left/right-scattering ratio is suspected to occur in a spectral region in between these resonance peaks, where the intrinsic phase differs by $\pi/2$, see Figure 5.2. In order to further improve the crystal quality of the gold nanodisks, the samples were annealed at 250 °C for 10 min. Even though this temperature is far below the melting point of gold, it is still sufficiently high to smooth the nanoparticle surface and make the crystalline grains large enough to overcome the mean-free-path of surface electrons. Hence this promotes lower dissipation and results in more narrow spectral resonance scattering peaks.

5.1.3 Microscope back-focal imaging for directionality quantification

By using incident loosely focused white light, by a low-magnification microscope objective (air 10×, NA = 0.3), polarized perpendicular with respect to the dimer axis, plasmonic dipoles were excited in a manner similar to what is described in Chapter 2.2. The transmitted and diffusely scattered light was then collected by the ultrahigh numerical aperture TIRF objective (oil 60×, NA = 1.49), which ensures nearly maximal collection efficiency. The Fourier images were measured by a SLR camera (Nikon D300s) using a 4f correlator, see illustration in Figure 5.1 (b).

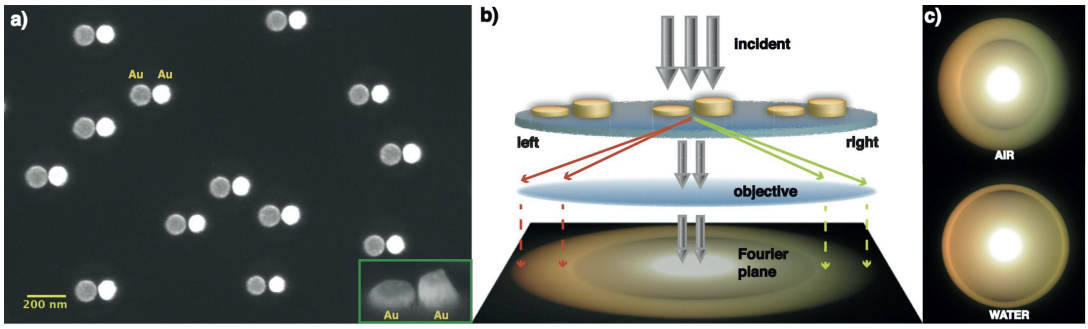

Figure 5.1: (a) *SEM image of asymmetric nanodimers comprised by Au nanodisks with different aspect ratio. The inset displays a tilted view on an isolated dimer.* (b) *Graphical scheme displaying the concept behind Fourier plane imaging.* (c) *Fourier plane images of scattered light from asymmetric Au nanodimers when either air or water constitutes the surrounding environment. Picture taken from [49].*

The directionality from the asymmetric dimers is so evident that it is clearly visible by

the naked eye, with reddish light scattering more efficiently to the left than to the right along the dimer axis. Moreover, apparent alterations of the Fourier image occur when the upper dielectric medium is changed from air to water, see Figure 10 (c), which is a strong indication that the setup is promising for refractometric sensing and analysis.

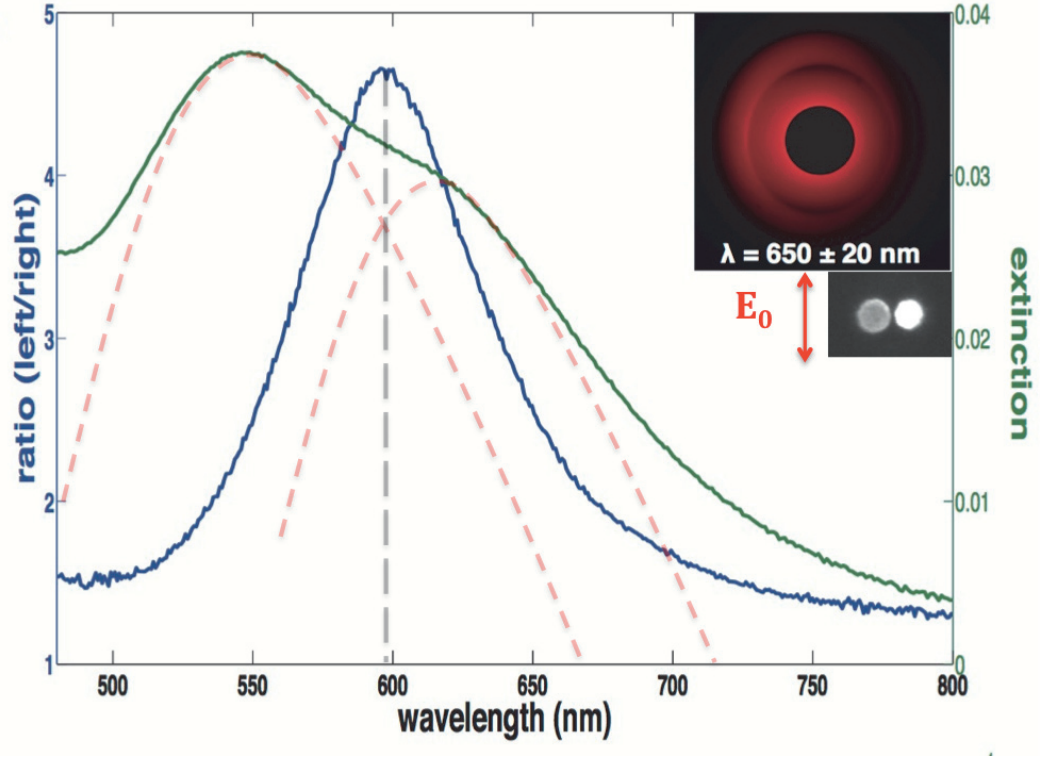

Figure 5.2: *Extinction and ratio of scattered intensities spectra combined to visualize that the maximum ratio occur at a point where the scattering of the two disks in the dimer is comparable and their intrinsic phase differs by $\pi/2$. Image taken from [49]*

5.1.4 Macroscopic spectrometer-free optical setup for molecular analysis

The incident white light was linearly polarized perpendicular to the dimer axis and delivered to the sample by a fiber and a collimating lens. The spot size (~5 mm) at the sample was controlled by a tunable iris aperture placed right after the collimating lens. The sample was in this case mounted inside a flow cell (chamber volume 0.5 mL) in order to have the ability to alter the ambient dielectric local environmental conditions.

The collection optics consisted of either a hemispherical or right-angle prism attached to the outer surface of the flow cell using index-matched oil which acts as a prolongation of the glass substrate. The light scattered at angles greater than critical from both sides of the prism was collected by two opposite optical fibers (400 μm core) and the resulting beams were simultaneously imaged on a CCD chip (Andor). A 650 nm (40 nm bandwidth) color filter was installed in front of the sample to mimic a simple spectrometer-free performance. The intensity of the light at the sample (after passing the filter) was measured to be 500 μW.

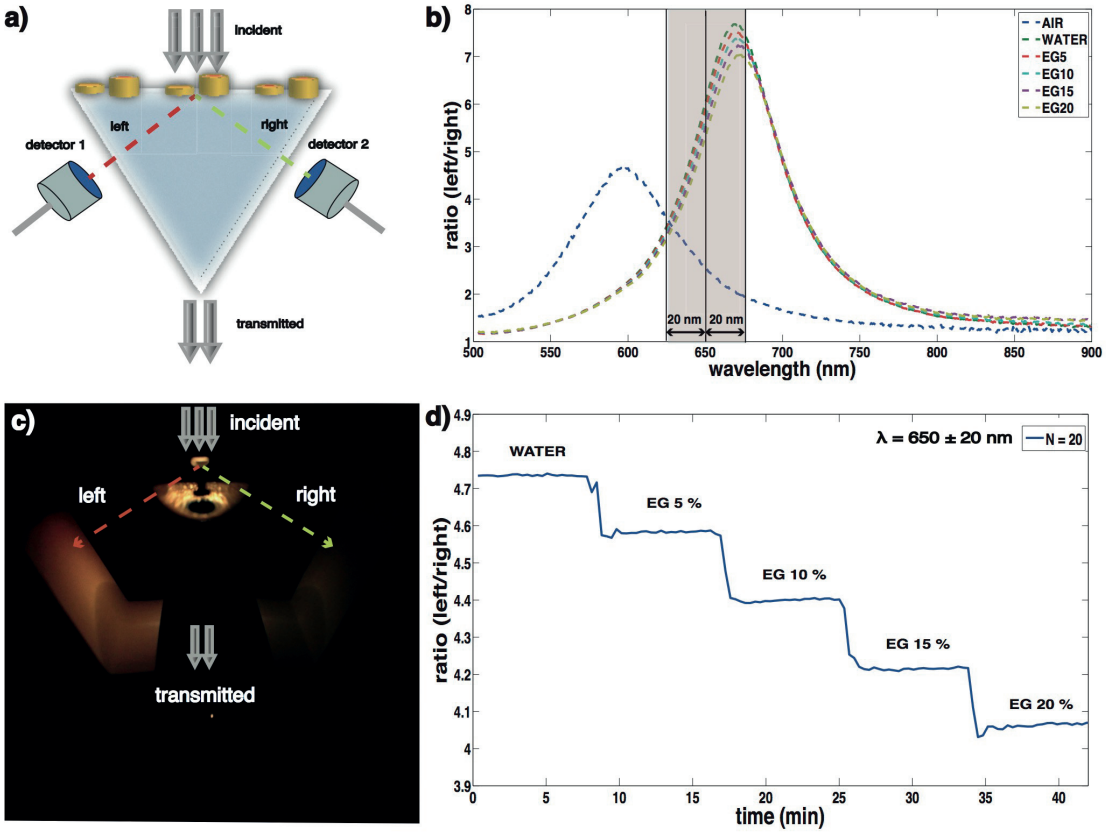

Figure 5.3: (a) *Schematic drawing of the microscope-free optical setup for directional single-wavelength refractometric sensing.* (b) *Change in spectral information of ratio from left/right-scattered intensities when the bulk refractive index is altered.* (c) *Photograph showing obvious directionality effect when paper sheets are placed in front of each detector.* (d) *Time-resolved single-wavelength (650±20 nm) refractometric bulk sensing using different concentrations of ethylene glycol. Picture taken from [49].*

A schematic description of the spectrometer-free setup can be seen in Figure 5.3 a, where both detectors are positioned at angles exceeding the critical angle of the lower/upper medium interface. In addition, bulk sensing data is depicted in Figure 5.3 b, d with spectral and single-wavelength measuring strategies respectively. The alteration in refractive index of each solution is performed by mixing various concentrations of ethylene glycol (EG) in water. Due to the documented fact that a 10% increase in EG concentration give rise to $\Delta n = 0.01\ RIU$ change in refractive index [50], the response in ratio could be well correlated with changes in the dielectric environment.

In addition to the previously described bulk-sensing model, local refractometric molecular analysis was performed to study binding kinetics in a biotin-neutravidin recognition model, see Figure 5.4. The dimers were first immersed in phosphate-buffer saline (PBS) to mimic the osmolarity and ion concentration of the human body fluids [51]. Secondly a 100 µg/ml of bio-conjugated bovine serum (bBSA) solution is injected into the flow cell and a slight decrease in the scattering ratio is observed. In this process bBSA molecules attach to the surface of the Au disks. Finally solutions of either 10 or 100 µg/ml concentrated neutravidin solutions were injected to the flow cell and a further decrease in ratio is observed that truly resembles ordinary molecular

binding kinetics [ref].

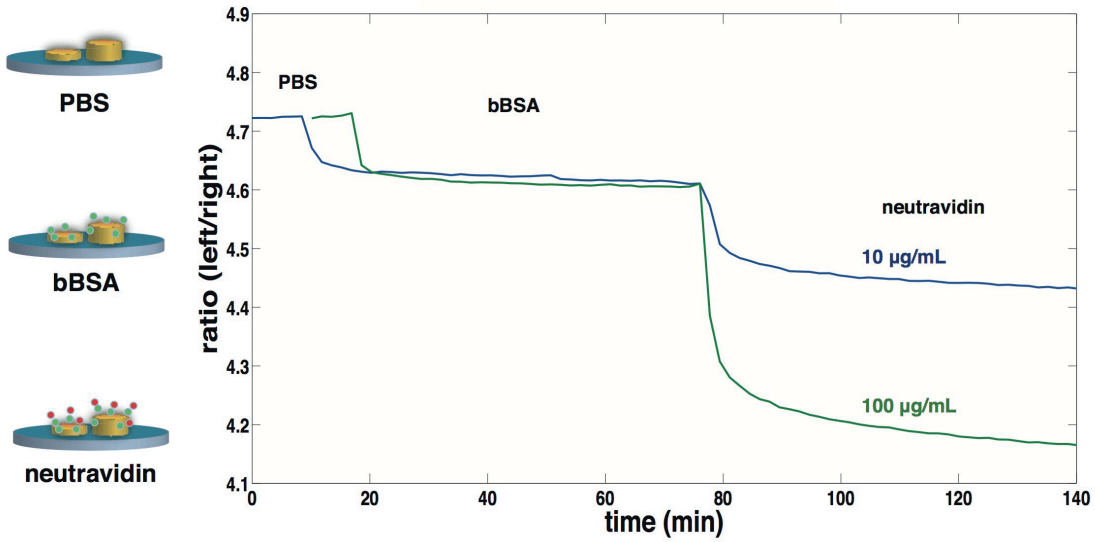

Figure 5.4: *Local refractometric sensing based on ratio of left/right-scattered intensities from asymmetric plasmonic nano antennas. The measurements are further conducted using a single-wavelength source of 650±20 nm. Image taken from [49].*

In order to quantify how sensitive this scheme is to alterations in the local dielectric environment, estimations was conducted based on the single-wavelength refractometric bulk sensing response together with the present noise-levels. The bulk sensitivity were measured and extracted to be $s = 37\ RIU^{-1}$ with noise-levels in the order of $\sigma_R \approx 1.86\times10^{-3}$. From these values it is possible to define a refractometric resolution parameter according to $\Delta n = {}^{\sigma_R}/_{S} \approx 5\times10^{-5} RIU$. These data was obtained from a measurement with $t = 20\ s$ per frame, integration time.

5.2 Coherent plasmon-exciton interaction for strong coupling

In this section the experimental methodology and implementation in relation to Paper II [52] are explicitly presented. Every step from devising the concept to fabrication of samples and the actual gathering of measurement data is thoroughly displayed.

5.2.1 J-aggregates of TDBC dye-molecules

The TDBC dye molecule is comprised by a rather complicated atomic structure (5,6-Dichloro-2- [[5,6-dichloro-1-ethyl-3- (4-sulfobutyl)-benzimidazol-2-ylidene]-propenyl]-1-ethyl- 3-(4-sulfobutyl) benzimidazolium hydroxide, inner salt, sodium salt). The formation of J-aggregate structure from monomers occurs in solution and depends on a number of factors including dye concentration, ionic environment and pH. A lowering of resonance energy is obtained when the molecules arrange themselves in a head-to-tail configuration, which give rise to a distinct narrow optical resonance peak located at 588 nm. This new configuration consists of strongly coherently coupled TDBC monomers which give rise to optical excitation delocalization and hence also an enhancement in transition dipole moment [53].

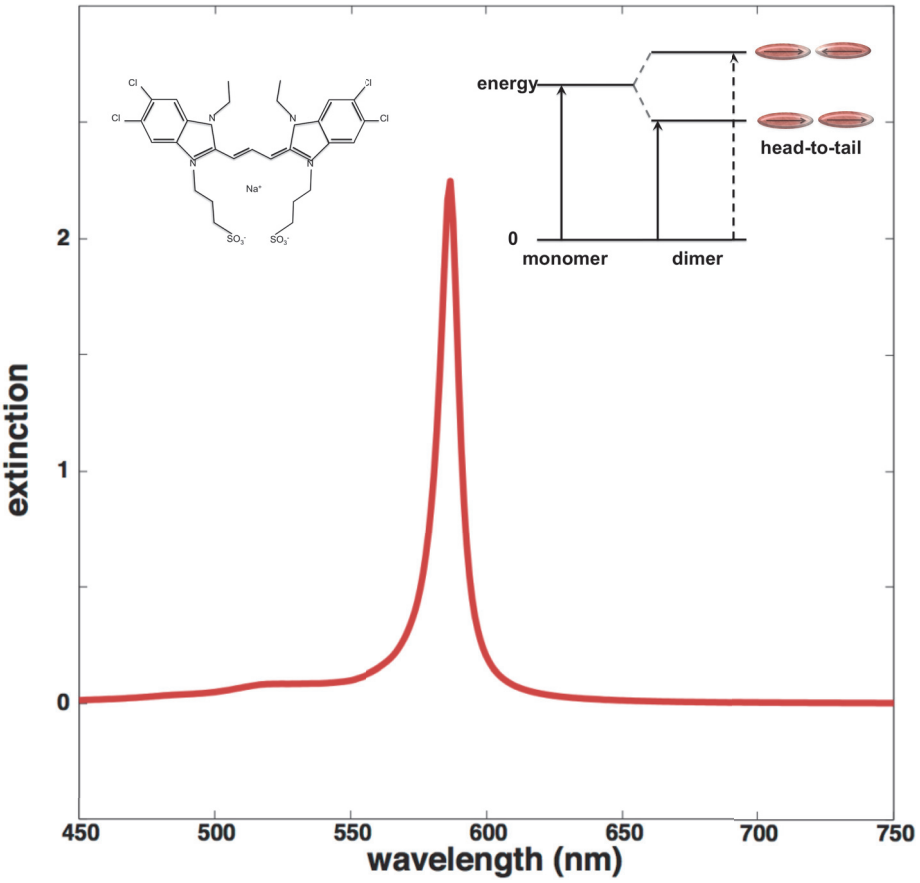

Figure 5.5: *Extinction spectrum of TDBC molecules in water. Note the distinct J-aggregate line at 588 nm. (Top left) Molecular structure of the TDBC molecule. (Top right) Schematic of molecular configuration in J-aggregated structures.*

The delocalized exciton in J-aggregates is extended over an average of as many as fifteen TDBC monomers [54], which in addition to an increased transition dipole moment accounts for a pertinent narrowing of the absorption band with respect to uncoupled monomers. Extinction spectrum, molecular structure and molecular configurations in J-aggregated TDBC molecules are depicted in Figure 5.5.

5.2.2 Particle-dye hybrid sample preparation

The Ag colloidal particles were synthesized by a light-induced ripening process, which due to a certain chosen illumination time (~ 60 hours, 532 nm) produces single-crystalline nanoprisms with an average side length of 70 nm [55]. In order to optimize the parameters for J-aggregate formation, the aqueous solution of TDBC dye was prepared at concentration of ~ 10 µM in 5 mM sodiumhydroxide (NaOH). Furthermore, 50 µl of Ag solution was mixed with 50 µl of J-aggregate solution. The mixture was left for incubation overnight in order to get an increased probability of attachment between particle and dye-aggregates. In order to remove any free TDBC monomer or free J-aggregates, the solution was centrifuged at 5000 rcf for 5 minutes and the supernatant was replaced with purified water (MilliQ).

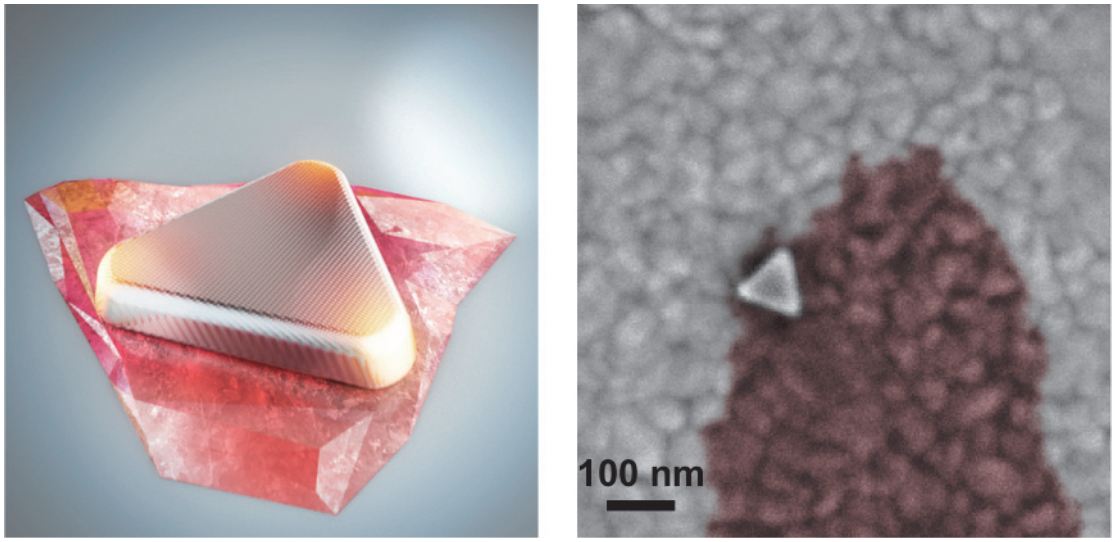

Figure 5.6: *(Left) Graphical image of the hybrid structure. A single crystalline Ag nanoprism in close contact with a sheet of J-aggregated TDBC molecules. (Right) SEM image of synthesized hybrid structure on top of a continuous gold film (grainy background). Images are taken from [52].*

The J-aggregate/Ag nanoparticles mixture was then applied to a TEM grid pre-coated with polylysine $(C_6H_{12}N_2O)_n$ to further improve adhesion between the particle-dye systems and the substrate. An illustration and an actual SEM image of the Ag nanoprism on top of a J-aggregate sheet are shown in Figure 5.6.

5.2.3 Optical measurements of scattering from single particle-dye systems

Single particle-dye hybrid systems were analyzed via dark-field scattering and fluorescence. All measurements were performed in an inverted microscope (Nikon TE-2000E) equipped with a tunable numerical aperture oil immersion objective (100X, NA = 0.5-1.3, Nikon). A tunable liquid crystal filter (VariSpec, 400-720 nm), that is transparent for light of only certain wavelength and linear polarization was used together with iXon EM-CCD detector (Andor) in order to perform hyperspectral imaging. Nearly isotropic in-plane polarization response of the nanoprisms justifies usage of the tunable filter in a single polarization channel. The transmission window of the liquid crystal filter was 10 nm, and was set to perform wavelength steps of 1 nm between successive images and synchronized with the CCD-camera via LabVIEW software. The hyperspectral images were recorded in sequences with a wavelength range from 500-720 nm and 535-650 nm for the dark-field and fluorescence measurements respectively. Only single nanoparticle data was analyzed in this study. In dark-field measurements, an air dark-field condenser (Nikon, NA = 0.8-0.95) was used together with a tungsten halogen lamp to illuminate the particle-dye systems.

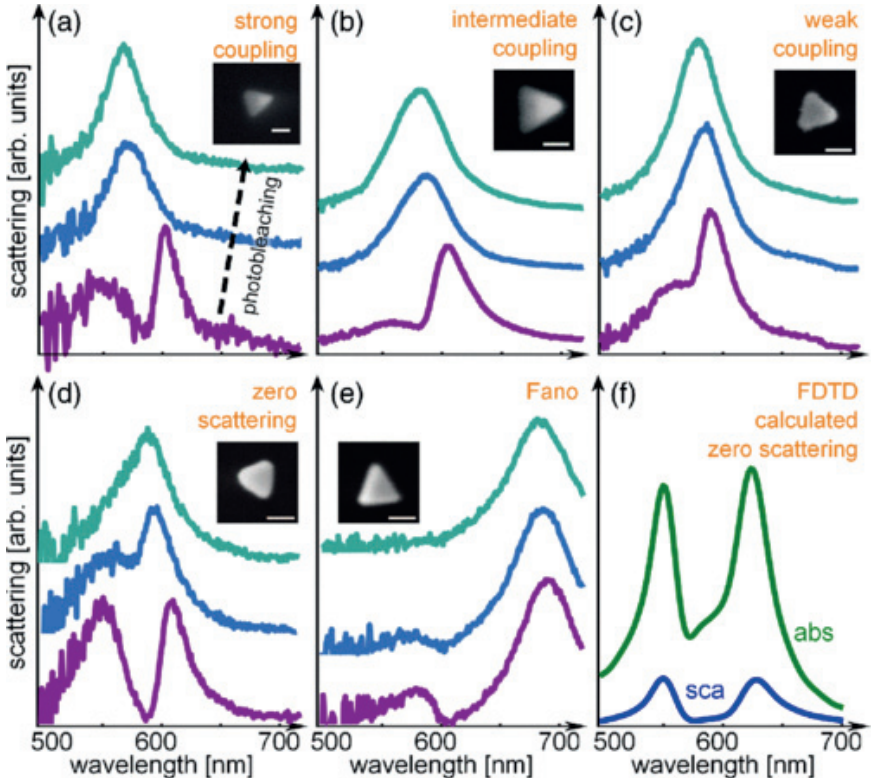

Figure 5.7: (a-e) *Dark-field scattering spectra from single Ag/J-aggregate systems showing a vareity of coupling regimes, each with SEM image of the corresponding plasmonic particle. The spectrum depicted in (f) is a FDTD simulation to mimic the case of zero scattering in both scattering and absorption. Image is taken from [52].*

The light intensity from the lamp was low enough to ensure no significant photo-degradation of the dye samples during the duration of the measurement. For fluorescence measurements, the sample was illuminated with a 532 nm laser at power of 100 W/cm^2 in epi-illumination mode in order to increase the laser spot size and hence collect fluorescence from a broader spatial area. The colored Rayleigh scattering and fluorescence images were taken by Nikon D300s DSLR camera. Various results obtained from the dark-field scattering measurements are shown in Figure 5.7, together with corresponding SEM images and signs of dye photo-decomposition.

5.2.4 Utilization of hyperspectral imaging

Experiments in this study were conducted by exploiting a hyperspectral imaging technique with a tunable liquid crystal filter. An overview of how hyperspectral imaging was utilized to extract spectral information is illustrated in Figure 5.8. Dark-field scattering images were recorded at a number of spectrally narrow intervals controlled by a tunable filter. The scattering spectrum was then reconstructed by monitoring the intensity of a given particle as a function of wavelength and was post-processed using a pre-written Matlab software programme. This procedure allows for parallel sampling of many isolated particles over the entire visible range and tremendously increases the throughput of single nanoparticle spectroscopy

measurements [56-57]. Dark-field scattering images of silver nanoparticles/J-aggregates hybrids recorded in this way are shown in the top row of Figure 5.8 (for five different exemplary wavelengths 500, 560, 580, 600, and 620 nm).

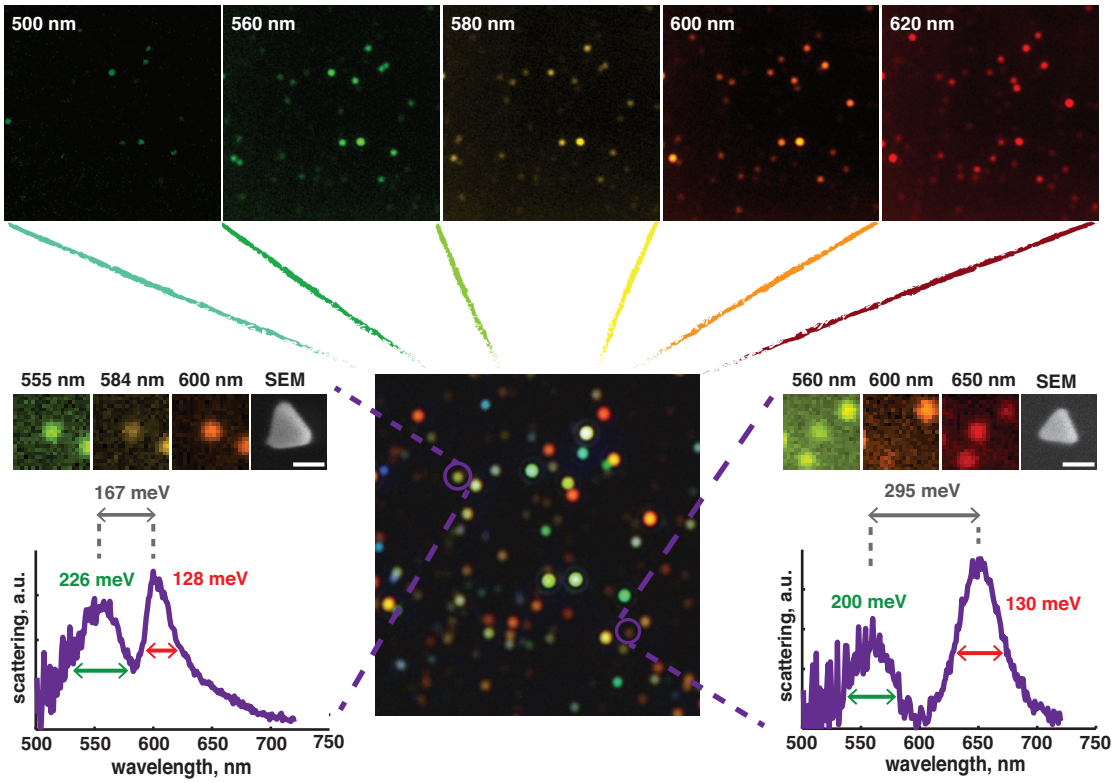

Figure 5.8: *A schematic image explaining how dark-field scattering spectra from single particle-dye systems are extracted from a two dimensional map utilizing hyperspectral imaging concept. SEM images of the corresponding Ag nanoprisms are furthermore also displayed. Image taken from [52].*

The images are approximately 35×35 μm. Two representative single nanoprism spectra together with their SEM images are shown. The particle on the left part of the figure exhibits a suppressed scattering at around the J-aggregate resonance wavelength (588 nm); however, the mode splitting does not overcome the plasmon resonance width, and the overlap between the hybrid modes are not negligible. The particle on the other side of the image, shows much wider splitting which clearly overwhelms both plasmon and molecular decoherence and dissipation rates and therefore enters the strong coupling regime. Vacuum Rabi splitting for this particle-dye system reaches about 300 meV, well above the plasmon resonance width, as shown in Figure 5.8. These two particles, and the brief analysis of their spectral differences, aim at illustrating the power of hyperspectral imaging for single particle spectroscopy.

5.2.5 Correlation of dark-field and scanning electron microscopy images

To ensure single-particle performance, high-vacuum scanning electron microscopy (SEM) with 2 kV acceleration voltage was used for imaging the single nanoparticles. Note that the dye-molecules were destroyed by the electron beam and could not be visualized under the current circumstances. As described in the sample preparation

section, the particles were applied on top of a copper-grid substrate containing several distinct hollow quadrants. Each quadrant was supported with a very thin membrane (formvar) on which the particles finally landed. Furthermore, in the center of the copper-grid, an asymmetric alignment mark was present which enabled us to locate and map out the quadrant of interest. Each particle inside a given quadrant was correlated with a corresponding optical image, based on which a correlated SEM-optical map was obtained. Since this step is crucial to claim that the spectra in fact originated from single particle-dye system, it is one of the most important parts of this whole study.

Chapter 6

Summary and Future Outlook

It has been shown in this thesis that coherent interactions at the nanoscale may be used in order to achieve refractometric molecular analysis via directional emission between two detuned plasmonic antennas, as well as strong coupling interactions between molecular excitons and a single plasmonic cavity.

In the case of performing refractometric analysis, based on directional emission, the demonstrated system is operating at a single-wavelength self-referenced manner with the ability to resolve refractometric alterations in the local dielectric environment around $\Delta n \approx 10^{-5} RIU$. A value comparable to several state-of-the-art systems based on plasmonic sensing [58]. Moreover, the system was built using compact and cheap optical component and had the ability to operate without any microscope or spectrometer, which further supress factors such as cost and inconvenient spacing [49].

Furthermore, strong light-matter interactions was demonstrated exploiting plasmon-exciton coupling in a system comprised by a single-crystalline Ag nanoprism and J-aggregated TDBC molecules. In this study vacuum Rabi energy splittings of 300 meV, with a splitting-to-cavity-dissipation ratio on the order of $\Omega_R/\gamma_{pl} \sim 1.5$ [52].

From these demonstrations it is obvious that coherent interactions at the nanoscale offers versatile possibilities for future applications in areas such as refractometric molecular analysis and room temperature quantum plasmonics and quantum optics.

6.1 Non-linearities in a cavity coupled to a single quantum emitter

The data corresponding to strong coupling due to plasmon-exciton interactions presented within this thesis rely on systems were several excitons ($N \sim 80$) coherently exchanges energy with the plasmonic cavity.

In order to observe non-linearities in line with what is described in Figure 4.1, systems comprised by a resonating cavity coupled to single or a few quantum emitters needs to be investigated [19]. There is still a rather big challenge to obtain single emitter hybrid systems with high enough coupling strength to overcome the dissipation rates in the system. However, with high enough transitition dipole moment of the quantum emitter and sufficiently low mode volume of the plasmonic cavity one may, according to (4.4) reach a coupling strength that is adequate to enter a strong coupling regime.

Furthermore the energy ladder, depicted in Figure 4.1, is highly dependent on number of cavity excitations N_{pl}. When exploiting plasmonic cavities the excitations have a lifetime in the femtosecond range [58]. This implies that one needs to externally excite the system with a high enough intensity source that will result in an irradiance corresponding to more than one photon per plasmon lifetime. For this purpose we aim to utilize a pulsed white-light laser with a side illumination of 45 degrees (oil immersion objective 100×, NA=0.5) in order to mimic non-linear dark-field scattering.
By comparing the dark-field scattering spectra obtained by the linear tungsten lamp and the non-linear white-light laser, one may be able to conclude if the single hybrid

systems support any non-linear photo dynamics.

6.2 Temperature controlled nanoscopic scattering suppression

The spectral linewidth of emission lines narrows for certain quantum dots when the surrounding temperature is decreased [59], especially when reaching cryogenic temperatures such as liquid helium (4 K). Spectral linewidths, originating from plasmonic cavities, on the other hand or not very much affected by an alteration in temperature [60]. The coupling strength in (4.4) is moreover independent on temperature. With all this in mind, the plasmon-exciton coupling dynamics from a semi-classical coupled-harmonic oscillator approach, results in that the spectral dip at the the isolated quantum emitter resonance scales as [17]

$$s = \frac{g}{\sqrt{\gamma_0 \gamma_{pl}}} \tag{6.1}$$

By keeping the parameters g and γ_{pl} constant while decreasing γ_0 sufficiently, the spectral dip, described by (6.1), and hence also the suppression of scattering will be very much affected.

Hence we want to investigate if it is possible to construct nanoscale hybrid system that support temperature controlled scattering suppression, due to plasmon-exciton interaction. Initial studies have already been performed on system comprised by a Au nanocube resting on top of a atomically flat continuous Au surface, with quantum dots positioned inside the gap region, see Figure 6.1. Due to the presence of the Au film the out-of-plane LSPR mode will interact strongly with its mirror image, inducing a strong field-enhancement inside the gap region [61-62], and hopefully couple strongly to the quantum dots.

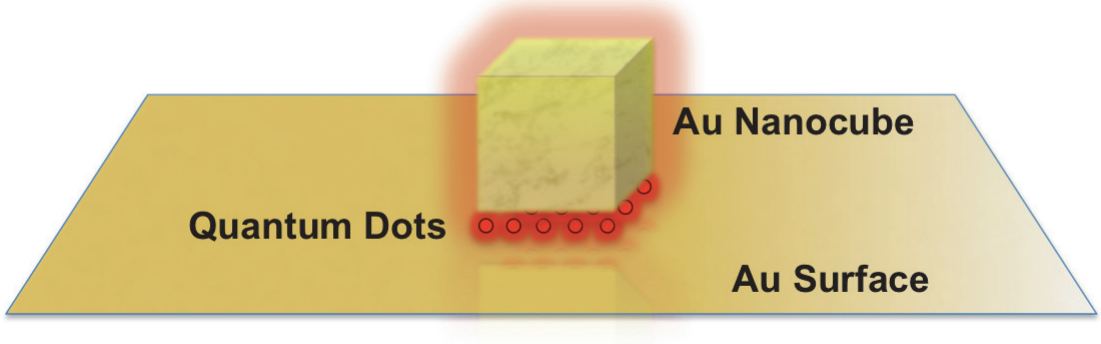

***Figure 6.1**: Graphical illustration of a hybrid system comprised by a plasmonic Au nanocube on top of a atomically flat contuous Au film, with quantum dots positioned inside the gap region.*

This model will be continued, investigated and developed during the upcoming future and we have high expectations that much of our theoretical predictions regarding the coupling dynamics will resemble the experimental outcomes.

Acknowledgements

I would like to take the opportunity to thank several colleagues and other people, whom have been encouraging and supporting during these projects.

First and foremost, I would like to dedicate a special thank you to my supervisor Dr **Timur Shegai** who has been encouraging, enthusiastic, patient and helpful throughout my entire work. You are a true source of inspiration and I am truly grateful for having the opportunity to work with you.

Professor **Mikael Käll**: Thank you for being encouraging and invigorative regarding the projects, and for all material support.

Dr **Gülis Zengin**: Thank you for teaching me many experimental skills, such as single particle dark-field scattering measurements and fluorescent microscopy. Thank you also for all fruitful discussions and inputs regarding every project aspect.

Dr **Ruggero Verre**: Thank you for very nice discussions regarding every aspect of the projects. Thank you for always being helpful and collaborating and always providing me with nice samples.

Dr **Mikael Svedendahl**: Thank you for your experimental expertise and help with sensing experiments, and also for profitable discussions regarding various aspects of my projects.

Dr **Tomasz Antosiewicz**: Thank you for your help and discussions regarding theoretical simulations of plasmon-exciton systems, and help in general in understanding plasmon dynamics.

Dr **Lei Shao**: Thank you for all help and support regarding chemistry, synthesis, experimental systems etc.

Kunli Xiong: Thank you for very fruitful discussions on plasmonics in general and sharing your views and comments on specific matters.

Gustav Emilsson: Thank you for nice and rewarding discussions regarding chemistry and plasmonic sensing.

Bionanophotonics Group: Thank you all for being great collegues and for nice and fruitful discussions and inputs regarding my research.

Dr **Anders Kvist**: Thank you for all help and support with SEM. Thank you for all the time you have been patient when I have bothered you with questions.

Jan-Åke Wiman: Thank you for always providing me with alternated optical components and devices, and also suggesting practical solutions to our experimental setups.

Alexander Ericsson: Thank you for all your help regarding graphics and figure design to the publication of Paper II.

Dr **André Dankert**: Thank you for helping out with AFM measurements on the particle-dye systems.

Dr **Annika Altskär**: Thank you for all help regarding the cryo-TEM measurements of J-aggregates.

Dr **Stefan Gustafsson**: Thank you for everything you provided regarding TEM measurements.

My father **Claes Wersäll**: Thank you for always being encouraging and supportive of my work. You always had a true interest for my projects even though you only understood a tiny part of what I was doing.

My mother **Margareta Wersäll**: Thank you for being constantly supportive and caring throughout my entire life.

Finally I would also like to thank **Knut and Alice Wallenberg Foundation** and the **Swedish Foundation of Strategic Research (SSF)**.

References

[1] J. Weiner & F. Nunes, *Light-Matter Interaction: Physics and Engineering at the Nanoscale*. Oxford: Oxford University Press, **2012**.

[2] Y. R. Shen, *Principles of Non-linear Optics*. New York: Wiley-Interscience, **1984**.

[3] E. F. Schubert, T. Gessmann, and J. K. Kim, *Light-Emitting Diodes*. New York: Kirk-Othmer Encyclopedia of Chemical Technology, **2005**.

[4] J. Nelson, *The Physics of Solar Cells*. London: Imperial College Press, **2003**.

[5] L. Vaidman, *Many-Worlds Interpretation of Quantum Mechanics*. Stanford: Stanford Encyclopedia of Philosophy, **2015**.

[6] J. Faye, *Copenhagen Interpretation of Quantum Mechanics*. Stanford: Stanford Encyclopedia of Philosophy, **2014**.

[7] E. Hecht, *Optics: 4th Edition*. Boston: Addison-Wesley, **2001**.

[8] L. Novotny & B. Hecht, *Principles of Nano-Optics*. New York: Cambridge University Press, **2006**.

[9] C. Bohren & D. Huffman, *Absorption and Scattering of Light by Small Particles*. New York: John Wiley & Sons, **1998**.

[10] N. J. Halas, *Plasmonics: An Emerging Field Fostered by Nano Letters*. Nano Letters, **2010**, 10, 3816-3822.

[11] H. Fredriksson, Y. Alaverdyan, A. Dmitriev, C. Langhammer, D. S. Sutherland, M. Zäch, and B. Kasemo, *Hole-Mask Colloidal Lithography*. Advancd Materials, **2007**, 19, 4297-4302.

[12] T. Shegai, M. Svedendahl, S. Chen, A. Dahlin, M. Käll, *Nanoantennas for Refractive Index Sensing*. In: M. Agio & A. Alù, *Optical Antennas*. New York: Cambridge University Press, **2013**, p. 340-356.

[13] J. Bellessa, C. Bonnand, and J. C. Plenet, *Strong Coupling between Surface Plasmons and Excitons in an Organic Semiconductor*. Physical Review Letters, **2004**, Vol. 93, 3.

[14] S. Balci, *Ultrastrong Plasmon-Exciton Coupling in Metal Nanoprisms with J-aggregates*. Optics Letters, **2013**, 38, 4498.

[15] J. Dintinger, S. Klein, F. Bustos, W. L. Barnes, and T. W. Ebbesen, *Strong Coupling between Surface Plasmon-Polaritons and Organic Molecules in Subwavelength Hole Arrays.* Physical Review B, **2005**, 71, 035424.

[16] W. Ni, T. Ambjörnsson, S. P. Apell, H. Chen, and J. Wang, *Observing Plasmonic-Molecular Resonance Coupling on Single Gold Nanorods*. Nano Letters, **2010**, 10, 77.

[17] G. Zengin, G. Johansson, P. Johansson, T. J. Antosiewicz, M. Käll, and T. Shegai, *Approaching the Strong Coupling Limit in Single Plasmonic Nanorods Interacting with J-aggregates*. Scientific Reports, **2013**, 3:3074.

[18] T. J. Antosiewicz, S. P. Apell, and T. Shegai, *Plasmon-Exciton Interactions in a Core-Shell Geometry: From Enhanced Absorption to Strong Coupling*. ACS Photonics, **2014**, 1 (5), pp 454-463.

[19] K. Hennessy, A. Badolato, M. Winger, D. Gerace, M. Atatüre, S. Gulde, S. Fält, E. L. Hu, and A. Imamoglu, *Quantum Nature of a Strongly Coupled Single Quantum Dot-Cavity System*. Nature (London), **2007**, 445, 896.

[20] S. Gröblacher, T. Paterek, R. Kaltenbaek, C. Brukner, M. Zukowski, M. Aspelmeyer, and A. Zeilinger, *An Experimental Test of Non-Local Realism*. Nature (London), **2007**, 446, 871.

[21] A. Imamoglu, D. D. Awschalom, G. Burkard, D. P. DiVincenzo, D. Loss, M. Sherwin, and A. Small, *Quantum Information Processing Using Quantum Dot Spins and Cavity QED*. Physical Review Letters, **1999**, 83, 4204.

[22] H. K. Lo and H. F. Chau, *Unconditional Security of Quantum Key Distribution Over Arbitrarily Long Distances.* Science, **1999**, 283, 2050.

[23] T. Volz, A. Reinhard, M. Winger, A. Badolato, K. J. Hennessy, E. L. Hu, and A. Imamoglu, *Ultrafast All-Optical Switching by Single Photons*. Nature Photonics, **2012**, 6, 605.

[24] Online Etymology Dictionary, www.etymonline.com, **2001-2015**.

[25] R. G. Driggers, *Encyclopedia of Optical Engineering*. Florida: CRC Press, **2003**.

[26] G. B. Folland, *Fourier Analysis and its Applications*. Providence: American Mathematical Society, **1992**.

[27] M. Meier & A. Wokaun, *Enhanced Fields on Large Metal Particles: Dynamic Depolarization*. Optics Letters, **1983**, 8, 11.

[28] V. D. Miljkovic, T. Pakizeh, B. Sepulveda, P. Johansson, and M. Käll, *Optical Forces in Nanoparticle Dimers*. The Journal of Physical Chemistry C, **2010**, 114, 7472-7479.

[29] W. Lukosz & R. E. Kunz, *Light Emission by Magnetic and Electric Dipoles Close to a Plane Interface. II. Radiation Patterns of Perpendicular Oriented Dipoles. Optical Society of America*, **1977**, 67, 1615-1619.

[30] B. H. Bransden & C. J. Joachain *Physics of Atoms and Molecules: 2nd Edition*. Harlow: Pearson Education Limited, **2003**.

[31] J. J. Sakurai & J. Napolitano, *Modern Quantum Mechanics, 2nd Edition*. New York: Pearson Publishing Co., **2010**.

[32] D. Bera, L. Qian, T. Tseng, and P. H. Holloway, *Quantum Dots and Their Multimodal Applications: A Review*. Materials, **2010**, 3, 2260-2345.

[33] M. D. Leistikow, J. Johansen, A. J. Kettelarij, P. Lodahl, and W. L. Vos, *Size-Dependent Oscillator Strength and Quantum Efficiency of CdSe Quantum Dots Controlled Via the Local Density of States*. Physical Review B, **2009**, 79, 045301.

[34] K. Henzler-Wildman & D. Kern, *A Hierarchy of Timescales in Protein Dynamics is Linked to Enzyme Catalysis*. Nature, **2007**, 450, 964-972.

[35] E. M. Larsson, C. Langhammer, I. Zoric, and B. Kasemo, *Nanoplasmonic Probes of Catalytic Reactions*. Science, **2009**, 326, 1091-1094.

[36] A. G. Brolo, *Plasmonics for Future Biosensors*. Nature Photonics, **2012**, 6, 709-713.

[37] J. N. Anker, W. P. Hall, O. Lyandres, N. C. Shah, J. Zhao, and R. P. Van Dyune, *Biosensing with Plasmonic Nanosensors*. Nature Materials, **2008**, 7, 442-453.

[38] D. A. Giljohann & C. A. Mirkin, *Drivers of Biodiagnostic Development*. Nature, **2009**, 462, 461-464.

[39] C. C. Gerry & P. L. Knight, *Introductory Quantum Optics*. New York: Cambridge University Press, **2005**.

[40] M. Keck, M. M. Müller, T. Calarco, and S. Montangero, *Quantum Optimal Control within the Rotating-Wave Approximation*. Physical Review A, **2015**, 92, 033402.

[41] E. T. Jaynes & F. W. Cummings, *Comparison of Quantum and Semiclassical Radiation Theories with Application to the Beam Maser*. Proceedings of the IEEE, **1963**, 51, 1, 89-109.

[42] X. Wu, S. K. Gray, and M. Pelton, *Quantum-dot-induced Transparency in a Nanoscale Plasmonic Resonator*. Optics Express, **2010**, Vol. 8, No. 23.

[43] A. E. Schlather, N. Large, A. S. Urban, P. Nordlander, and N. J. Halas, *Near-Field Mediated Plexitonic Coupling and Giant Rabi Splitting in Induvidual Metallic Dimers*. Nano Letters, **2013**, 13, 3281-3286.

[44] J. M. Torres, *Closed-Form Solution of Lindblad Master Equation Without Gain*, Physical Review A, **2014**, 89, 052133.

[45] B. M. Garraway, *The Dicke Model in Quantum Optics: Dicke Model Revisited*. Philosophical Transactions of the Royal Society A, **2011**, 369, 1137-1155.

[46] A. B. Evlyukhin, S. I. Bozhevolnyi, A. Pors, M. G. Nielsen, I. P. Radko, M. Willatzen, and O. Albrektsen, *Detuned Electrical Dipoles for Plasmonic Sensing*. Nano Letters, **2010**, 10, 4571-4577.

[47] T. Shegai, S. Chen, V. D. Miljkovic, G. Zengin, P. Johansson, and M. Käll, *A Bimetallic Nanoantenna for Directional Colour Routing*, Nature Communications, **2011**, 2:481.

[48] T. Shegai, P. Johansson, C. Langhammer, and M. Käll, *Directional Scattering and Hydrogen Sensing by Bimetallic Pd-Au Nanoantennas*. Nano Letters **2012**, 2464-2469.

[49] M. Wersäll, R. Verre, M. Svedendahl, P. Johansson, M. Käll, and T. Shegai, *Directional Nanoplasmonic Antennas for Self-Referenced Refractometric Molecular Analysis*. The Journal of Physical Chemistry C, **2014**, 118 (36), pp 21075-21080.

[50] The MEGlobal Group of Companies. *Product Guide: Ethylene Glycol*, **2008**, p. 25.

[51] E. D. Hendry, *Osmolarity of Human Serum and of Chemical Solutions of Biologic Importance.* Clinical Chemistry, **1961**, Vol. 7, No. 2, 156-164.

[52] G. Zengin, M. Wersäll, S. Nilsson, T.J. Antosiewicz, M. Käll, and T. Shegai, *Realizing Strong Light-Matter Interactions between Single Nanoparticle Plasmons and Molecular Excitons at Ambient Conditions*. Physical Review Letters, **2015**, 114, 157401.

[53] R. C. Hilborn, *Einstein Coefficients, Cross Sections, f-Values, Dipole Moments, and All That*. American Journal of Physics, **1982**, 50, 982.

[54] M. Van Burgel, D. A. Wiersma, and K. Duppen, *The Dynamics of One-Dimensional Excitons in Liquids*. Journal of Chemical Physics, **1995**, 102, 20.

[55] R. Jin, Y. Cao, C. A. Mirkin, K. L. Kelly, C. G. Schatz, a J. G. Zheng, *Photoinduced Conversion of Silver Nanospheres to Nanoprisms*. Science, **2001**, 294, 1901.

[56] J. M. Bingham, K. A. Willets, N. C. Shah, D. Q. Andrew, and R. P. Van Duyne, *LSPR Imaging: Simeltaneous Single Nanoparticle Spectroscopy and Diffusional Dynamics*. Journal of Physical Chemistry C, **2009**, 113, 16839.

[57] S. Chen, M. Svedendahl, R. P. Van Duyne, and M. Käll, *Plasmon-Enhanced Colometric ELISA with Single Molecule Sensitivity.* Nano Letters, **2011**, 11, 1826-1830.

[58] Y. S. Yi, *Integrated Nanophotonic Resonators: Fundamentals, Devices, and Applications*. Florida: CRC Press, **2015**.

[59] W. Ouerghui, A. Melliti, M. A. Maaref, and J. Bloch, *Dependence on Temperature of Homogeneous Broadening of InGaAs/InAs/GaAs Quantum Dot Fundamental Transitions*. Physica E, **2005**, 519-524.

[60] M. Liu, M. Pelton, and P. Guyot-Sionnest, *Reduced Damping of Surface Plasmons at Low Temperatures*. Physical Review B, **2009**, 79, 035418.

[61] M. Hu, A. Ghoshal, M. Marquez, and P. G. Kik, *Single Particle Spectroscopy of Metal-Film-Induced Tuning of Silver Nanoparticle Plasmon Resonances*. The Journal of Physical Chemistry C, **2010**, 114, 7509-7514.

[62] J. J. Mock, R. T. Hill, A. Degiron, S. Zauscher, A. Chilkoti, and D. R. Smith, *Distance-Dependent Plasmon Resonant Coupling between a Gold Nanoparticle and a Gold Film*. Nano Letters, **2008**, Vol. 8, No. 8, 2245-2252.